

# Regular Pattern Detection and Analysis Using Shapelets

by

Robert Suderman

A thesis  
presented to the University of Waterloo  
in fulfillment of the  
thesis requirement for the degree of  
Master of Mathematics  
in  
Computer Science

Waterloo, Ontario, Canada, 2014

© Robert Suderman 2014

I hereby declare that I am the sole author of this thesis. This is a true copy of the thesis, including any required final revisions, as accepted by my examiners.

I understand that my thesis may be made electronically available to the public.

## Abstract

The presence of regular patterns in natural and technological phenomena is pervasive, often being present in both time and space. To increase our understanding of many phenomena where patterns are present, measurable quantities or metrics are typically defined and used for quantitative analysis. In many fields of study, methods for robustly computing these metrics do not exist, impeding further progress in these areas. Self-assembled materials is one area where significant advances in microscopy techniques have enabled the generation of detailed imaging of self-assembled domains. Unfortunately, image analysis methods to quantify self-assembly patterns in this imaging data either do not exist or are severely limited in their applicability. With the ability to acquire this data but not quantify it, scientists and engineers face significant challenges in determining relationships between structure and properties of these materials.

In this work, a generalized method for the quantitative analysis of pattern images is developed which addresses many of the existing challenges, specifically for the field of self-assembled materials. The presented method is based upon a family of localized functions called *shapelets* and is fundamentally different from existing approaches. The method is composed of sets of shapelets reformulated to be “steerable” filters and a guided machine learning algorithm. We demonstrate using realistic surface self-assembly data that this approach is able to *quantitatively* distinguish between uniform (defect-free) and non-uniform (strained, defects) regions within the imaged self-assembled domains. In addition to being a fundamental departure from existing pattern analysis methods, we show that the presented method provides a generalized (pattern agnostic) analysis method with significantly enhanced resolution (pixel-level) compared to existing techniques (pattern feature-level).

## **Acknowledgements**

I would like to thank both of my supervisors, Dan Lizotte and Nasser M. Abukhdeir, for their guidance, enthusiasm, and patience throughout the duration of this research project. Without their support, the method contained within these pages would be a shadow of its current scope. Also, thank you to Chengbo who consistently made himself available to discuss the approaches in this thesis and provide feedback on the presentation of image processing methods to those inexperienced with its techniques.

# Table of Contents

List of Tables	vii
List of Figures	viii
<b>1 Introduction</b>	<b>1</b>
1.1 Self-Assembly and Nanotechnology	2
1.2 Thesis Statement	6
1.2.1 Contributions	6
<b>2 Background</b>	<b>8</b>
2.1 Spectral Analysis	8
2.1.1 Two-Dimensional Discrete Fourier Transform	9
2.2 Convolutions	12
2.2.1 Relationship to the Fourier Transform	13
2.2.2 Use in Image Processing	14
2.2.3 Orienting Filters	15
2.3 Shapelets	16
2.4 Bond Orientational Order Theory	18
<b>3 Theory and Application of Shapelets to the Analysis of Surface Self-assembly Imaging</b>	<b>21</b>
3.1 Global Periodic Scale	22

3.2	Sets of Steerable, Scale-Optimized Shapelets . . . . .	23
3.2.1	Pattern Symmetries . . . . .	24
3.2.2	Rotational Invariance . . . . .	25
3.2.3	Scaling . . . . .	26
3.3	Application to Self-Assembly Imaging . . . . .	28
3.4	Conclusions . . . . .	31
<b>4</b>	<b>Improved Analysis using Orientation Extraction</b>	<b>34</b>
4.1	Comparison of Sets of Steerable Shapelet Filter Responses . . . . .	35
4.2	Orientation-Enhanced Comparison of Sets of Steerable Shapelets . . . . .	37
4.2.1	Application to Self-Assembly Imaging . . . . .	39
4.3	Conclusions . . . . .	41
<b>5</b>	<b>Conclusions</b>	<b>42</b>
5.1	Conclusions . . . . .	42
5.2	Recommendations . . . . .	42
<b>A</b>	<b>Appendices</b>	<b>44</b>
A.1	Shapelet Proofs . . . . .	44
A.1.1	Lemma 1 . . . . .	44
A.1.2	Lemma 2 . . . . .	45
A.2	Additional Sample Images . . . . .	47
	<b>References</b>	<b>55</b>

# List of Tables

3.1	Coefficient values for $\beta = C\lambda$ for shapelets up to order six. . . . .	28
-----	--	----

# List of Figures

1.1	Schematics of patterns composed of discrete features . . . . .	1
1.2	Sample images of patterns with indistinct or uncertain features . . . . .	3
1.3	Schematics of surface patterns with features composed of collective domains of particles/atoms . . . . .	4
1.4	Example of a (simulated) hexagonal self-assembled film and local hexagonal order resulting from applying the bond orientational order method . . . . .	5
2.1	Fourier Shift: Shifting the spectral density allows frequencies to be grouped into circles around the image centre. In figure (c), the distance $r$ from the image centre represents frequency, and the brightness reflects the amplitude of the original image at that frequency. . . . .	12
2.2	Polar shapelets . . . . .	17
2.3	Schematic images of a (a) continuous surface pattern, (b) the binary data resulting from thresholding of the continuous surface pattern; (c) the nearest-neighbour graph where convex pattern features are used as vertices and edges are created using Delauney triangulation. . . . .	18
2.4	Different types of bond-orientational order analysis of the surface pattern shown in Figure 2.3 . . . . .	19
2.5	Bond-orientational pattern orientation of the surface pattern shown in Figure 2.3 . . . . .	20

3.1	Fourier transform: We observe the original pattern in 3.1a with the magnitude of the Fourier Transform in 3.1b. The radial spectral density is shown in 3.1c with LOESS smoothed amplitude over frequencies. Note that although Figure 3.1a is not a pure sinusoid, the sinusoidal components of the figure are highly concentrated in a ring at a frequency of approximately $27 \text{ nm}^{-1}$ , which is clearly visible in both the 2D spectral density 3.1b and the radially-averaged spectral density 3.1c. . . . .	22
3.2	Sample Synthetic Patterns generated from Equation 3.1. . . . .	24
3.3	Plots of one-mode approximations . . . . .	25
3.4	Shapelet filter response versus $\beta$ . . . . .	27
3.5	Responses of steerable polar shapelet filters applied to uniform one-mode approximations . . . . .	29
3.6	Examples of hexagonal surface self-assembly with features of varying character	30
3.7	Examples of non-uniform striped and hexagonal patterns from simulations of surface self-assembly and results from applying the guided machine learning algorithm to them . . . . .	33
4.1	Localized reconstructions of two hexagonal pattern regions indicated in 4.1a are shown in in 4.1b and 4.1c. This process is repeated for a striped pattern with regions shown in 4.1d with reconstructions in 4.1e and 4.1f. . . . .	36
4.2	Optimal rotated reconstructions . . . . .	38
4.3	Applying the new approach to the hexagonal pattern in 3.7d we obtain a measurement of material quality in 4.3a. The orientation value $\theta$ is shown in 4.3b using a color with the value $(R, G, B) = (\sin(\theta), \sin(\theta + 2\pi/3), \sin(\theta + 4\pi/3))$ . . . . .	40
4.4	Applying the new approach to the striped pattern in 3.7a we obtain a measurement of material quality in 4.4a. The orientation value $\theta$ is shown in 4.3b using a color with the value $(R, G, B) = (\sin(\theta), \sin(\theta + 2\pi/3), \sin(\theta + 4\pi/3))$ . . . . .	41
A.1	A hexagonal pattern formed in a simulation of surface self assembly. This figure provides a comparison between the Chapter 3 and Chapter 4 approaches.	47
A.2	A striped pattern formed in a simulation of surface self assembly. This figure provides a comparison between the Chapter 3 and Chapter 4 approaches. . . . .	48

A.3	A synthetically generated hexagonal pattern with changing orientation. This figure provides a comparison between the Chapter 3 and Chapter 4 approaches.	49
A.4	A synthetically generated striped pattern with changing orientation. This figure provides a comparison between the Chapter 3 and Chapter 4 approaches.	50
A.5	A synthetically generated hexagonal pattern with varying noise. This figure provides a comparison between the Chapter 3 and Chapter 4 approaches.	51
A.6	A synthetically generated striped pattern with varying noise. This figure provides a comparison between the Chapter 3 and Chapter 4 approaches.	52
A.7	A synthetically generated image containing both a striped and hexagonal pattern. This figure provides a comparison between the Chapter 3 and Chapter 4 approaches.	53
A.8	A synthetically generated image containing both a striped and hexagonal pattern with a different pattern sample. This figure provides a comparison between the Chapter 3 and Chapter 4 approaches.	54

# Chapter 1

## Introduction

The presence of regular patterns in natural and technological phenomena is pervasive, often manifested spatially and temporally. To increase our understanding of phenomena where patterns are present, we require measurable qualities for quantitative analysis. Focusing on spatial patterns, there are typically distinct features or objects which are the atomic units that form the pattern under a periodic relationship, re-tiling the pattern over a larger domain. Figure 1.1 shows examples of patterns formed by varying the arrangement of the discrete objects.

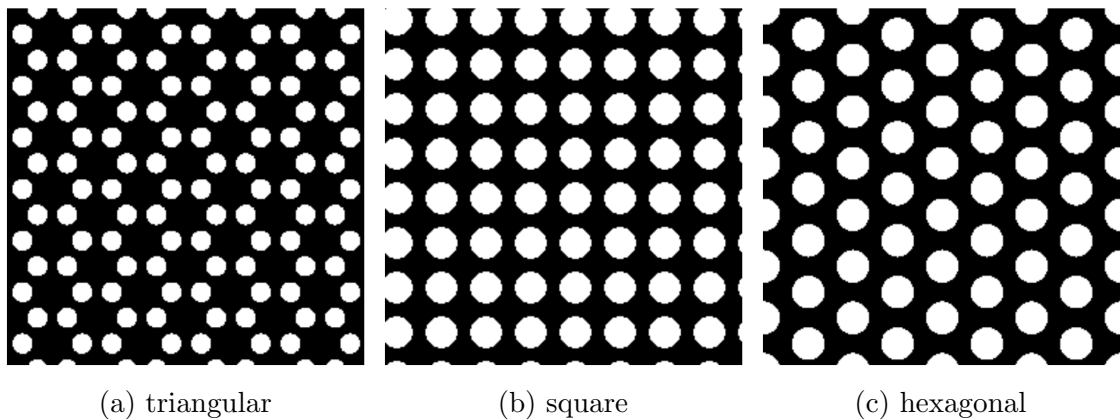


Figure 1.1: Schematics of patterns composed of discrete features: (a) triangles, (b) squares, (c) hexagons.

One method for quantifying a pattern with discrete pattern features (e.g. the “dots” in

Figure 1.1) is to identify, for each feature, how many “nearest neighbours” it has<sup>1</sup> and then describe how those neighbours are arranged around each pattern feature. When pattern features are discrete, or can be well-approximated as discrete, both local and global metrics can be defined to quantify a pattern in this way using bond-orientational order (BOO) theory [1]. BOO theory defines a sequence of order parameters ( $\Psi_n$ ) for each feature and the orientation of the edges between a feature and its nearest neighbours,

$$\Psi_n = \frac{1}{N} \sum_{i=1}^N \exp(ni\phi) \quad (1.1)$$

where  $N$  is the number of nearest neighbours of a pattern feature<sup>2</sup>,  $n$  is the number of vertices on an individual feature and  $\phi$  is the angle representing orientation of the neighbour. The magnitude of  $\Psi_n$  quantifies the degree to which the pattern conforms to an  $n$ -fold symmetric spatial ordering, which in turn is a description of the pattern’s *regularity*.

Application of this theory enables quantification of both global (whole image) and local (within an image) pattern metrics, however challenges exist when applying BOO theory to pattern features that are not well-defined. In some circumstances, pattern features are obscured by the presence of noise or non-convex features. Figure 1.2 demonstrates a set of examples where the presence of noise makes separating features and determining centre points a difficult task, even though *the example patterns have important regularity as well*.

Figure 1.2a demonstrates an example of non-isolated features. As stripes do not possess a centre point, instead forming along a line, their presence cannot be described at a single central point. In Figure 1.2b there exists a significant measurement of uncertainty in the imaging data that increases the difficulty of determining image centres. In both of these cases, there is important pattern regularity that we would like to identify and describe (e.g. the frequency and orientation of the stripes) but the application of BOO theory is not possible without significant approximations.

## 1.1 Self-Assembly and Nanotechnology

Self-assembled materials are emerging [2] as a key enabler of “bottom-up” manufacturing techniques. Bottom-up manufacturing has the potential to significantly reduce the manufacturing costs compared to “top-down” techniques such as lithography. Research and

---

<sup>1</sup>Defined, for example, by its neighbours in a Delaunay triangulation.

<sup>2</sup>Assuming each pattern feature is associated with a well-defined “centre point” which is given.

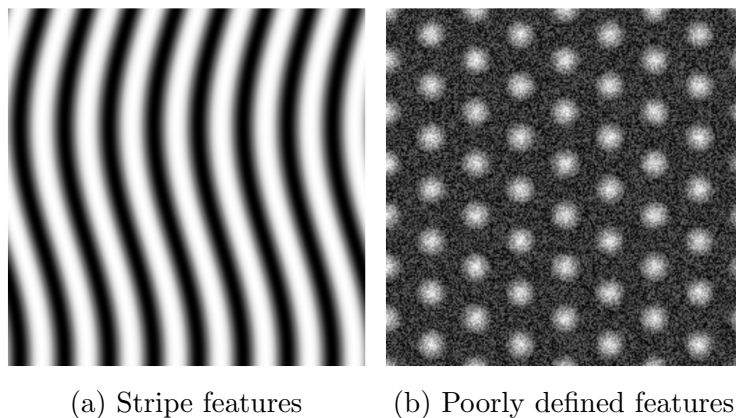


Figure 1.2: Sample images of patterns with indistinct or uncertain features: (a) stripe pattern that has features that are not localized (they are spread out vertically) and (b) hexagonal pattern with noise that makes the exact location of each pattern feature uncertain.

application of self-assembly phenomena has resulted in significant advances in microscopy techniques to generate images of self-assembled domains. These advances in microscopy techniques are producing an ever-increasing [3–5] amount of high-resolution imaging data of self-assembled materials, specifically surface self-assembled materials. With the ability to acquire this data, scientists and engineers face a new challenge in processing this imaging data to determine relationships between the structure and the quality of these materials. So far, BOO theory has been the only approach for the analysis of surface self-assembly imaging that has provided quantitative pattern metrics in both the global and local domains.

It has been previously [6] shown that there exist several limitations to BOO theory which are magnified for self-assembly imaging. Surface self-assembly films typically contain [7] nanoscale pattern features, resulting in highly uncertain imaging of these materials. Subsequently, identification of distinct features in a pattern requires a significant degree of filtering to remove noise and accurately detect features. Secondly, surface self-assembly typically [7] involves pattern features composed of many particles, which can result in highly complex and inherently indistinct pattern features. An example of this is shown in Figure 1.3, which is a schematic of a surface self-assembly with pattern features composed of thousands of individual atoms. These pattern features can vary significantly in their size and morphology while still conforming to the same overall pattern type (stripe, square, hexagonal, etc.).

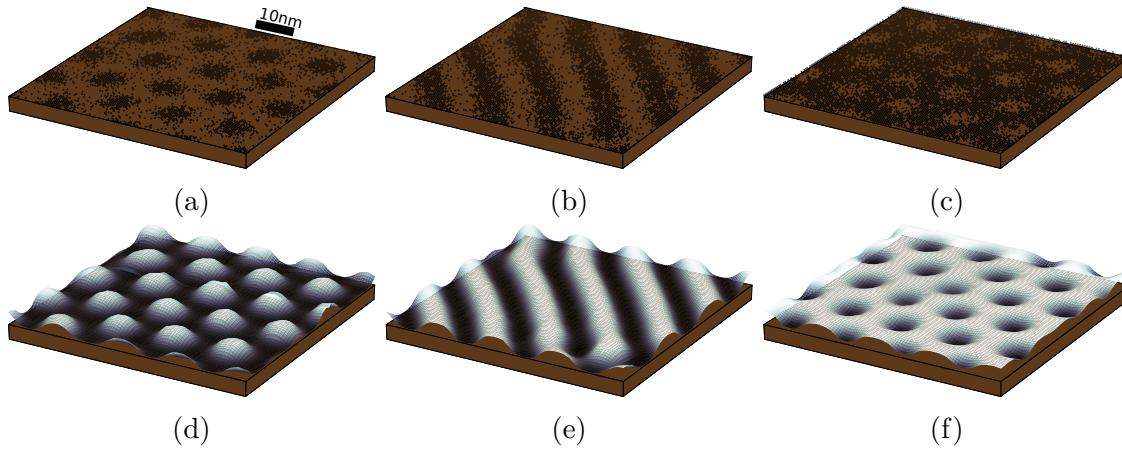


Figure 1.3: Schematics of surface patterns with features composed of collective domains of particles/atoms: (a) hexagonal, (b) stripe, and (c) inverse hexagonal; surface plots of image intensities resulting pattern-scale imaging of surface pattern (d-f). Taken from ref. [7]

One goal of pattern analysis is to identify which pattern features have a given symmetry (e.g. 6-fold) with respect to their nearest neighbours. To solve this problem, application of BOO theory to self-assembly images is possible in ideal cases, such as the example shown in Figure 1.4b. In this case, given an image with both known pattern (hexagonal) and convex pattern features, BOO theory gives an approach to compute both the feature–neighbour relationship and determine the pattern orientation. These relationships can then be used in conjunction with BOO theory [1] to approximate local pattern orientation and identify defects. This type of quantification of surface order has been vital in the identification of pattern evolution mechanisms and defect kinetics [7–11]. Despite the fundamental advances that BOO theory has enabled in the area of self-assembled materials, the BOO approach has many significant limitations specific to this area. In summary, these limitations are:

- *Resolution* – BOO theory quantifies order at the pattern “feature” level, where pattern features are sub-domains which repeat in an ordered way. Typically, these features are larger than the resolution of the image, as is the case in Figure 1.4a, which results in a coarse resolution of local pattern order as shown in Figure 1.4b where interpolation is used.
- *Convexity* – in order to compute *unique* nearest neighbour “bonds” between pattern features, the features must be convex. This precludes the use of the method on striped patterns and patterns in which features vary greatly in character (strained patterns).

- *Uncertainty* – in order to compute nearest neighbour “bonds” between pattern features, the location of each feature must be uniquely identifiable. Typical experimental images of self-assembly phenomena involve nanoscale features which result in significant measurement uncertainty.

Furthermore, images frequently contain multiple regions that may or may not contain patterns, or may contain multiple patterns. As a result, there is a clear need for a robust, automated approach to pattern recognition and classification for self-assembly imaging [12], in addition to a more detailed characterization once these initial questions have been answered.

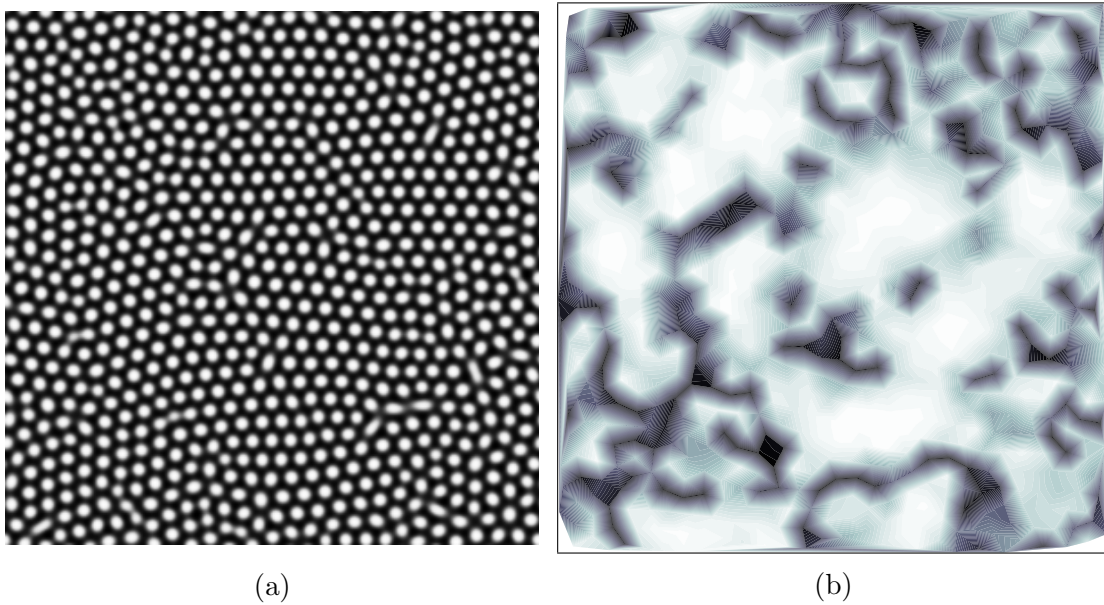


Figure 1.4: (a) Example of a (simulated) hexagonal self-assembled film from past work [13] where the field shows surface coverage of a species ranging from  $0 \rightarrow 1$ ; (b) interpolated magnitude of the local hexagonal order  $\Psi_6$  resulting from applying the bond orientational order method to (a). The magnitude ranges from no order, i.e. no six-fold symmetry (black) to perfect order, i.e. perfect six-fold symmetry (white). Taken from ref. [14]

BOO theory characterizes unordered regions using the number of adjacent neighbours for each feature in the image. For the hexagonal pattern shown in Figure 1.4b, unordered behaviour is observed by features possessing 5 or 7 neighbours. Examining the darkened regions we observe they correspond with instances of more or less than 6 neighbours.

## 1.2 Thesis Statement

The aim of this research is to develop a generalized method for the quantitative analysis of pattern images that addresses the limitations of BOO as described above, as applied to the analysis of surface self-assembly imaging.

The method that is developed is based upon a family of localized functions called *shapelets* [15] and is fundamentally different from that of BOO theory as the analysis is performed in a continuous method instead of identifying discrete features. Shapelet theory was originally developed to characterize images of galaxies ( $\propto 10^{20}$  m) [15] – they are used here to characterize images of nanoscale surfaces patterns ( $\propto 10^{-9}$  m).

### 1.2.1 Contributions

We demonstrated that, using realistic simulation data of self-assembled surfaces, the presented approach is able to robustly determine *local* pattern characteristics, using an appropriate subset of shapelets [15, 16] and steerable filter theory [17], such as sub-domains that are well-ordered, strained, and/or have defects present.

The main contributions to the thesis are summarized below:

1. *Shapelets as “Steerable” Filters (Chap. 3)* – We show that shapelets can be reformulated into “steerable” filters using steerable filter theory enabling computationally efficient determination of filter response with respect to orientation (rotation of the filter).
2. *Steerable Shapelets as Pattern Filters (Chap. 3)* – We show that the series of steerable shapelets up to order  $n$  may be reformulated to respond to a fixed scale, while maintaining orthogonality, into a set of filters whose response is maximal for surface patterns with  $n$ -fold symmetry.
3. *Local Pattern Classification (Chap. 4)* – We demonstrate using realistic surface self-assembly data that an approach resulting from the combination of steerable shapelet filters and guided machine learning is able to *quantitatively* distinguish between uniform (defect-free) and non-uniform (strained, defects) regions within the imaged self-assembled domains.

The shapelet-based method provides significantly enhanced resolution (pixel-level) compared to the bond-orientational order method (feature-level). Besides furthering fundamen-

tal understanding of self-assembly, these contributions will be key enablers of the ultimate goal of controlling self-assembly to produce task-optimized material properties [18].

# Chapter 2

## Background

This thesis is based on two standard techniques in image processing: spectral analysis [19] and convolution theory. Within convolution theory, this thesis uses a special classification of filters known as shapelets [15, 16] and a method for orienting these filters with steerable filter theory [17]. Finally, the existing method for characterizing self-assembly pattern analysis, bond orientational order theory [1], is summarized.

### 2.1 Spectral Analysis

Spectral analysis is a tool to quantify the periodic behaviour [19] present in a signal  $F$ . For a one-dimensional signal  $F[i]$ ,  $i \in \{0, \dots, n-1\}$ , this is achieved by decomposing  $F$  into sinusoidal functions with varying amplitudes, frequencies and phases. For a two-dimensional signal  $F[i, j]$ , which we think of as an *image*, the signal is decomposed into two-dimensional sinusoidal functions that have different amplitudes, frequencies, phases and directions. Identifying the dominant periodic behaviour in a discrete time signal is performed by projecting the signal onto the space of discrete frequencies across its domain and identifying frequencies with large amplitudes. For each frequency, an inner product is taken to determine both the amplitude and phase shift of the frequency. In the one-dimensional case, the projection

$$\hat{F}[\omega] = \sum_{i=0}^{n-1} F[i] e^{-2\pi i \frac{i}{n} \omega} \quad \omega = 0, \dots, n-1 \quad (2.1)$$

is given by inner products between the signal  $F$  and the set of discrete frequencies  $\omega$ , producing a measurement of the amplitude  $\hat{F}[\omega]$  at each frequency  $\omega$ . Here,  $i$  is the imaginary unit. This projection is known as a *discrete Fourier transform* (DFT) [20], which is the main tool used in spectral density analysis for both signal and imaging data.

The computational requirement for calculating the inner product for a single frequency  $\omega$  is directly proportional to the size of the discrete signal  $F$  ( $O(n)$ ), where  $n$  is the size of the signal). As there are  $O(n)$  unique discrete frequencies across the domain<sup>1</sup>, a naive implementation to identify all unique discrete frequencies is  $O(nm)$ . This runtime can be improved using a divide-and-conquer approach, reducing the computational complexity to  $O(n \log n)$ , this method is referred to as the *fast Fourier transform* (FFT) [20].

### 2.1.1 Two-Dimensional Discrete Fourier Transform

Generalizing a DFT to higher dimensions is achieved by quantifying periodicity along each dimension of the signal. For the two-dimensional case, the inner product is given by:

$$\hat{F}[x, y] = \sum_i^{n-1} \sum_j^{m-1} F[i, j] e^{-2\pi i (\frac{i}{n}x + \frac{j}{m}y)}. \quad x = \{0, \dots, n-1\} \quad y = \{0, \dots, m-1\}, \quad (2.2)$$

where  $[x, y]$  is a pair of frequencies, one along each dimension. Note that for each  $[x, y]$ , the naive computation of  $\hat{F}[x, y]$  requires  $O(n \cdot m)$  operations. However, after separating the summations along each dimension, the transform can be written as:

$$\hat{F}[x, y] = \sum_i^{n-1} e^{-2\pi i \frac{i}{n}x} \sum_j^{m-1} F[i, j] e^{-2\pi i \frac{j}{m}y} \quad x = \{0, \dots, n-1\} \quad y = \{0, \dots, m-1\}, \quad (2.3)$$

effectively decomposing the two-dimensional DFT into two sets of one-dimensional DFTs. The first set performs  $n$  one-dimensional DFTs of length  $m$  along one axis and the second set performs  $m$  one-dimensional DFTs of length  $n$  along the second axis. This allows the two-dimensional DFT to be computed using  $m + n$  one-dimensional DFTs decreasing the overall computational complexity to  $O(nm(\log n + \log m))$ .

The coefficients from two-dimensional DFT will be interpreted to analyze the patterns. In order to interpret the coefficients, the following properties of the two-dimensional DFT are reviewed:

---

<sup>1</sup>See ref. [20] for justification of why these are sufficient.

1. Complex coefficients
2. Sampling and shifting
3. Indices in two-dimensions

## Complex Coefficients

The result of a two-dimensional DFT of a non-symmetric signal yields a set of complex values [20] in frequency space, even when the signal  $F$  is real. This is because the complex exponential  $e^{ix}$  is equivalent to the form  $\cos(x) + i \sin(x)$ . When transforming real-valued data, at each frequency  $\omega$ , the real component of  $\hat{F}[\omega]$  corresponds to the cosine strength and the imaginary component of  $\hat{F}[\omega]$  corresponds to the sine strength at that frequency. The real part of a complex number is denoted by  $\Re[\bullet]$  and the imaginary part is denoted by  $\Im[\bullet]$ . Given  $\hat{F}[\omega]$ ,  $F$  has a sinusoidal component given by

$$\Re[\hat{F}[\omega]] \cos i + \Im[\hat{F}[\omega]] \sin i \quad (2.4)$$

The summation of a sine and cosine can be expressed as a single phase-shifted sinusoid of combined amplitude, thus it is possible to reinterpret the coefficients in  $F$  as an amplitude and a phase shift. Using the identity,

$$A \sin(i) + B \cos(i) = \sqrt{A^2 + B^2} \sin(i + \arctan(A, B)), \quad (2.5)$$

the Fourier coefficient  $\hat{F}[\omega]$  can be reinterpreted as the amplitude,

$$\sqrt{\Re[\hat{F}[\omega]]^2 + \Im[\hat{F}[\omega]]^2} \quad (2.6)$$

and the phase angle

$$\arctan(\Re[\hat{F}[\omega]], \Im[\hat{F}[\omega]]) \quad (2.7)$$

of the sinusoidal component with frequency  $\omega$ . In this research, the focus will be on the frequencies' amplitudes to determine the “dominant” amplitudes, i.e. frequencies that best describe the variation in  $F$ .

## Sampling and Shifting

When examining the coefficients of a two-dimensional DFT, it is useful for interpreting the data, to perform a horizontal and vertical translation of the data set by half the width and height, respectively. To understand the reason for this, an example in the one-dimensional case is presented. The domain of  $F$  is the integer values  $\{0, \dots, n-1\}$  and  $e^{k2\pi i} = 1$  for all integers  $k$ , thus given the discrete Fourier Transform

$$\hat{F}[\omega] = \sum_{i=0}^{n-1} F[i] e^{-2\pi i \frac{i}{n} \omega} \quad (2.8)$$

$$(2.9)$$

We can multiple by  $e^{i2\pi i}$  which equals 1 when  $i$  is an integer

$$= \sum_{i=0}^{n-1} F[i] e^{i2\pi i} e^{-2\pi i \frac{i}{n} \omega} \quad (2.10)$$

$$(2.11)$$

Combining the exponential components

$$= \sum_{i=0}^{n-1} F[i] e^{-2\pi i \frac{i}{n} (\omega - n)} \quad (2.12)$$

$$(2.13)$$

We can observe the relationship between Fourier coefficients.

$$= \sum_{i=0}^{n-1} F[i] \overline{e^{-2\pi i \frac{i}{n} (n-\omega)}}. \quad (2.14)$$

For real  $F$ , the coefficients  $\hat{F}[\omega]$  when  $\omega \geq n/2$  are *conjugate symmetric* [20] to those of the lower order frequencies of the same magnitudes. Translating both  $x$  and  $y$  components of the two-dimensional DFT such that the constant valued component (i.e. the component at  $[x, y] = [0, 0]$ , also referred to as the ‘‘DC component’’) is centred at the origin allows coordinates near and far from the origin to be interpreted as ‘‘low frequencies’’ and ‘‘high frequencies,’’ respectively. Therefore, the Fourier transform is defined as:

$$\hat{F}[x, y] = \sum_{i,j} F[i, j] e^{-2i\pi \left( \frac{i-n/2}{n} x + \frac{j-m/2}{m} y \right)}. \quad (2.15)$$

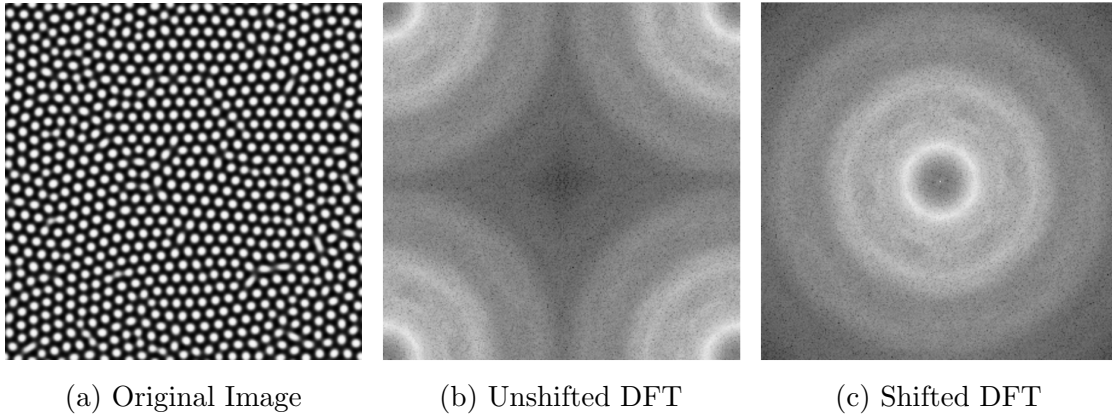


Figure 2.1: Fourier Shift: Shifting the spectral density allows frequencies to be grouped into circles around the image centre. In figure (c), the distance  $r$  from the image centre represents frequency, and the brightness reflects the amplitude of the original image at that frequency.

### Indices in Two-Dimensions

Each coordinate of the two-dimensional Fourier transform as defined in Equation (2.15) is identified with a pair of frequencies,  $x$  and  $y$ , which describe the rate of oscillation in the  $i$  and  $j$  directions in the original signal, respectively. These pair of frequencies can be reinterpreted as a single plane wave with frequency  $\omega$  and direction  $\phi$  given by

$$\phi = \arctan(x, y) \quad \omega = \sqrt{x^2 + y^2}. \quad (2.16)$$

This can be interpreted as a transformation from Cartesian to polar coordinates in frequency space. A radial average of the new two-dimensional Fourier transform is used to evaluate the importance of a particular frequency independently from image orientation; i.e. the average of  $F$  over  $\phi$  at constant  $\omega$  is examined. This analysis of frequencies will be thoroughly covered in Section 3.1.

## 2.2 Convolutions

A common tool for detecting specific characteristic localized patterns in images are *convolutions*. Convolutions can also be used to enhance or remove certain behaviour in an image. A convolution is an inner product between an input image and a weighting function, often referred to as a *filter*, through all discrete translations. The result of performing

a convolution is a new function with the same dimensions as the inputs. Formally, the convolution is given by,

$$(F \otimes G)[x, y] = \sum_i \sum_j F[i, j] \cdot G[x - i, y - j], \quad (2.17)$$

which shows the relationship between each indexed value and the input values, along with its relationship with the inner product.

Convolutions possess a number of useful properties, they are commutative, associative and distributive. The commutative property allows the filter and target image to be interchanged without changing the result. The associative property allows filters to be linearly combined to form new hybrid filters, and using distributivity we can evaluate the response of these new filters by using the same linear combination of their response. The value of convolution  $F \otimes G$  at a point  $[x, y]$  can also be viewed as a measure of similarity between  $F$  and  $G$  when the filter is translated to that point in the image. This idea is central to our work in subsequent chapters, where we will use the convolution operation to identify regions of an image that “match” our weighting functions.

### 2.2.1 Relationship to the Fourier Transform

Performing a convolution directly from its definition can be prohibitively expensive. In the case of a two-dimensional convolution there are  $O(n^2)$  values in the input and output arrays. Evaluating each location requires performing a translated two-dimensional inner product between both input arrays, requiring  $O(n^2)$  for each inner product and producing a total runtime of  $O(n^4)$  to compute every value. Due to the computational complexity in performing this operation there exist a variety of methods for improving the overall runtime. However, due to a special relationship between convolutions and the Fourier transform, there is a computation method that is more efficient. Due to the orthogonality relationship between discrete frequencies, a convolution can be performed in frequency space by multiplying sets of Fourier coefficients [20]. Since computing a Fourier transform of a two-dimensional image requires  $O(n^2 \log n)$  time, the overall runtime of this improved convolution becomes bound by performing the Fourier transform, which drastically improves on the naive approach.

This computational improvement also introduces a separate interpretation for a convolution. Taking the Fourier transform of the filter and image produces sets of coefficients to be multiplied together for the convolution. The process of multiplying these coefficients together can be interpreted as performing a phase shift and reweighing of each discrete

frequency in the image, according to the Fourier values in the filter. If the convolution is attempting to extract characteristic behaviour in the image, the multiplication of the Fourier coefficients enhances the frequencies that would define said behaviour and reduces non-characteristic behaviour of the filter.

### 2.2.2 Use in Image Processing

Convolutions are often used in image processing to detect whether some characteristic behaviour exists in a target image. A filter can be identified and convolved with the target image. The resulting output produces a table of values that correspond with the inner product values of the transposed filter and the image. Higher values are indicative of a strong similarity between image and filter. A zero value indicates no similarity and a negative value indicates similarity between the image and the negated version of the filter. As a result, convolutions are a common tool in classification algorithms, such as face or object recognition, as the convolution with a generic face filter will match positively when it is evaluated over a face present in an image. The advantage of using this technique over the squared error approach is that at each location, the convolution approach has a runtime of  $O(n^2 \log n)$ , while squared error has a runtime of  $O(n^4)$ .

Furthermore, it can be shown that there exists a relationship between the inner product computed as part of the convolution and the squared error between the image and the filter. The squared error between two arrays can also be evaluated by taking the magnitude of both arrays and subtracting the inner product between the two arrays. Therefore measuring the squared error between two images can be evaluated by taking the convolution between one image and the transposed version of the other image, negating and adding the magnitude of both images. The benefit of this observation is that maximizing the inner product is equivalent to minimizing the squared error [21]. As a result, squared error can be efficiently evaluated over two-dimensional images  $F$  and  $G$

$$err = \sum_i \sum_j (F[i, j] - G[i, j])^2 \quad (2.18)$$

as follows: Expanding the contents of the summation.

$$err = \sum_i \sum_j (F[i, j]^2 + G[i, j]^2 - 2F[i, j]G[i, j]) \quad (2.19)$$

We can simplify the sum of squared components  $F$  and  $G$  as their squared norm.

$$err = |F|^2 + |G|^2 - 2 \sum_i \sum_j F[i, j]G[i, j] \quad (2.20)$$

Finally we observe the remaining sum is equivalent to double the negative inner product between  $F$  and  $G$ .

$$err = |F|^2 + |G|^2 - 2F \cdot G \tag{2.21}$$

### 2.2.3 Orienting Filters

We will eventually wish to compare images with rotated versions of filters. However, convolutions only compare the image with translated versions of the filter. Finding the optimal translation *and orientation* of a filter — that is, the combined translation and rotation that produce the highest similarity — can be difficult as even finding the optimal filter rotation for a fixed translation may be a non-convex optimization problem, even for relatively simple filters. We discuss two approaches for finding the optimal rotation of a filter.

**Naive Optimization** Finding the maximum similarity at each location can be naively performed using multiple convolutions of varying orientation. This is performed by varying the orientation of the filter over a discrete grid and recording the value of the convolution of the image with the rotated filter at each location in the image. A search is conducted at each point for the rotation that gives the maximum similarity. Depending on the rotational resolution required, the number of required convolutions can be substantial.

**Steerable Filters** A collection of filters known as *steerable* filters were created to find special cases where the optimal rotation can easily be computed. Presented by Freeman et al. [17] and used often in computer vision [22], these filters are defined such that using the convolution results from a finite number of filters, a model can be constructed that gives a filter’s response under *any orientation* without re-evaluating the filter. Using the distributive property described in Section 2.2, it is known that if a filter can be constructed using a linear combination of component filters, the results of convolving the component filters with the image can be used to construct the result of convolving the original filter with the target image. Therefore, if a single rotated filter  $G(\theta)$ , can be expressed as a linear combination of sub filters  $g_i$  as shown in Equation (2.23), all possible orientations can be evaluated using the linear relationship. Let  $G(\theta)$  represent a filter that has been rotated through an angle  $\theta$ , and  $F$  be an image of interest. Also, suppose that  $G(\theta)$  can be

written as a linear combination of filters  $g_i$ , with weights  $\alpha_i(\theta)$  that depend on  $\theta$ . Then,

$$G(\theta)[x] = \sum_i \alpha_i(\theta) g_i[x], \quad (2.22)$$

$$F \otimes G(\theta) = \sum_i \left[ \alpha_i(\theta) \sum_x (g_i[x] \otimes F[x]) \right]. \quad (2.23)$$

Therefore,  $F \otimes G(\theta)$  can be evaluated at any  $\theta$  by first performing a convolution for each  $g_i$  and then taking their weighted sum as prescribed by the  $\alpha_i(\theta)$ . Often, the  $\alpha_i$  form simple functions (i.e. sinusoids) which can be efficiently maximized by solving for a zero derivative (shown below). Even in situations where a closed form solution does not exist, evaluating the response over an array of orientations has a substantially lower computational complexity.

$$\frac{d}{d\theta} F \otimes G(\theta) = \frac{d}{d\theta} \sum_i \alpha_i(\theta) [g_i \otimes F] = \sum_i \frac{d}{d\theta} \alpha_i(\theta) [g_i \otimes F] = 0 \quad (2.24)$$

## 2.3 Shapelets

In this work, a convolutions of input images with a family of filters referred to as *shapelets* are used. Shapelets were originally created for the deconstruction and classification of galaxies from astronomical imaging data [15, 16]. They were designed as a generalization of a Gaussian filter to produce a set of orthonormal filters that could be tuned for any size while also minimizing the effects of noise. For the scope of this work, only a sub family of *polar shapelets* with the simplified form shown in Equation (2.25) are used. We define the shapelet  $S_{m,n}^\beta(r, \theta)$  as constructed by the values of  $m$ ,  $n$ , and  $\beta$  over the space of polar coordinates  $(r, \theta)$ . The values  $m$  and  $n$  are the natural number indices that affect the periodic behaviour of the shapelets in the angular and radial directions, respectively. The last value  $\beta$  represents the shapelet scale, allowing the size of the measured behaviour to vary. The particular shapelets we use are given by

$$S_{m,n}^\beta(r, \theta) = C_{m,n}^\beta f_n^\beta(r) e^{im\theta} \quad (2.25)$$

where the function  $f_n$  in the above is the Laguerre polynomial of order  $n$  [15], and the scalar  $C_{m,n}^\beta = (\int f_n^\beta(r) e^{im\theta})^{-1}$  ensures that the shapelet integrates to unity.

**Indices** The indices of a shapelet define the overall shape it describes. In two-dimensional polar shapelets, they occur as a pair of natural number values,  $m$  and  $n$ , which each quantify a different form of complexity. The  $m$  value of a polar shapelet controls the degree of rotational symmetry and is varied in Figure 2.2 across the horizontal axis. The  $m$  value can be interpreted as the number of oscillations of the shapelet over a full rotation. The second index,  $n$ , represents the vertical axis of Figure 2.2 and describes the radial complexity measured by the shapelet. This can be considered as the number of oscillations of minima and maxima while moving away from the shapelet centre.

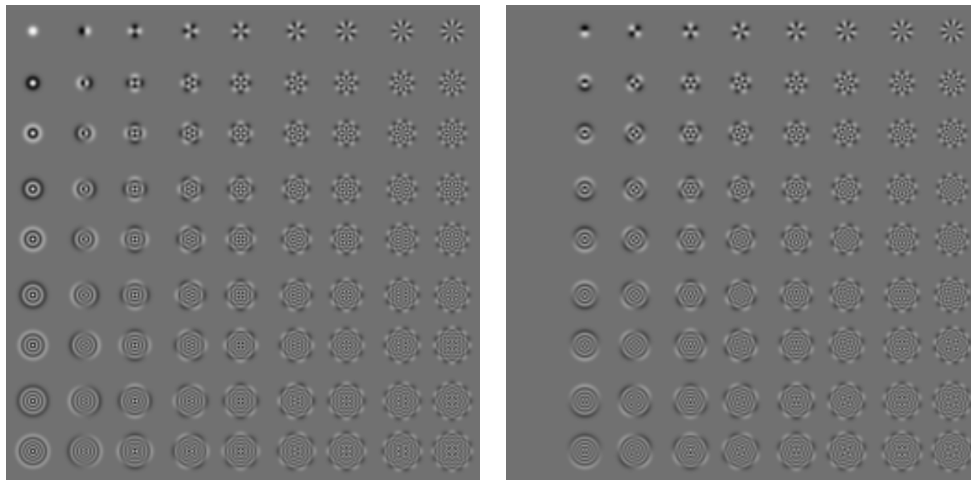


Figure 2.2: Polar shapelets. Horizontal indices represent an increase in rotational symmetry while vertical indices represent the radial symmetry. The left figure shows the real component, and the right panel shows the imaginary component.

**Scale** Constructing a shapelet also requires a scaling parameter,  $\beta$ . This parameter controls the overall scale that shapelet will be constructed at by manipulating the Gaussian component of the filter. Increasing this factor produces a shapelet that looks for large-scale shape of its behaviour, while decreasing it attempts to identify behaviour at a smaller scale. Using this parameter, a shapelet can be tuned to search for the same behaviour at any scale.

## 2.4 Bond Orientational Order Theory

Bond orientational order theory [1, 7, 23] enables the quantification of  $n$ -fold symmetric organization of discrete objects. It has been used in the natural sciences to quantify spatial order of discrete particles, such as atoms and molecules, that are spatially correlated, forming materials such as crystal lattices, liquid crystalline phases, and self-assembled materials. The basis for this method is the definition of a complex-valued order parameter  $\Psi_n$  for each discrete particle such that the magnitude of the order parameter increases as the spatial distribution of nearest neighbour particles conforms to  $n$ -fold symmetry,

$$\Psi_n = \frac{1}{N} \sum_{i=1}^N \exp(n\phi_i), \quad (2.26)$$

where  $N$  is the number of nearest neighbours of a pattern feature,  $\phi_i$  is the angle representing orientation of the “bond” or line segment between the feature and its  $i^{\text{th}}$  neighbour, and  $n$  is the symmetry of the pattern. Distances or length scales between particles are not explicitly considered. Instead, they are implicitly considered through the identification of nearest neighbour particles. Thus, the spatial configuration of particles may be represented using an undirected graph where vertices correspond to the centre of mass of particles and edges correspond to “bonds”. Figure 2.3 illustrates the relationship between a two-dimensional distribution of particles and its nearest neighbour graph.

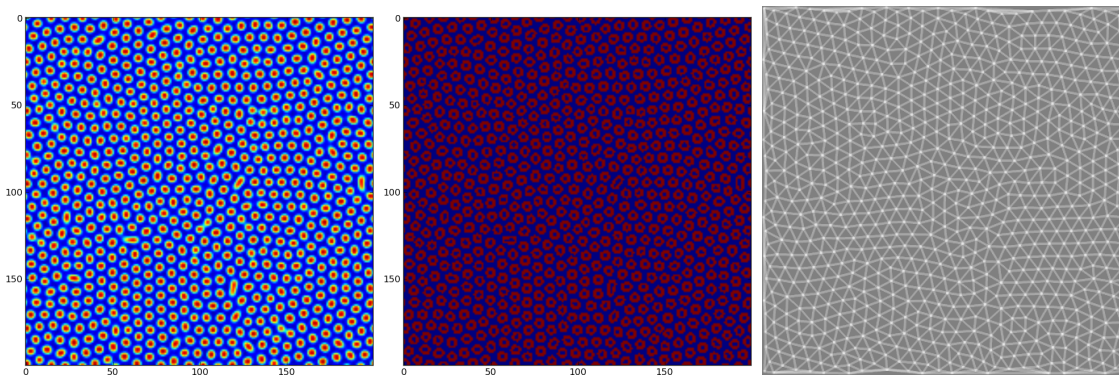


Figure 2.3: Schematic images of a (a) continuous surface pattern, (b) the binary data resulting from thresholding of the continuous surface pattern; (c) the nearest-neighbour graph where convex pattern features are used as vertices and edges are created using Delauney triangulation.

This relatively simple formalism enables quantitative analysis of both local and global pattern characteristics. First, the bond-orientational order parameter may be averaged over

each particle in the domain to yield a global measure of the degree of  $n$ -fold symmetric patterns present in an image. Figure 2.4a shows these quantities for the image shown in Figure 2.3a. Second, once the dominant pattern is identified, local bond-orientational order may be approximated through interpolation of the order parameter values defined at each point. Figure 2.4b shows the magnitude of the  $\Psi_6$  order parameter field for the image shown in Figure 2.3a. Finally, “defects” in the pattern may be identified through location of particles with nearest neighbours not equal to  $n$ . Figure 2.4b shows the location of particles which correspond to defects in the 6-fold pattern for the image shown in Figure 2.3a.

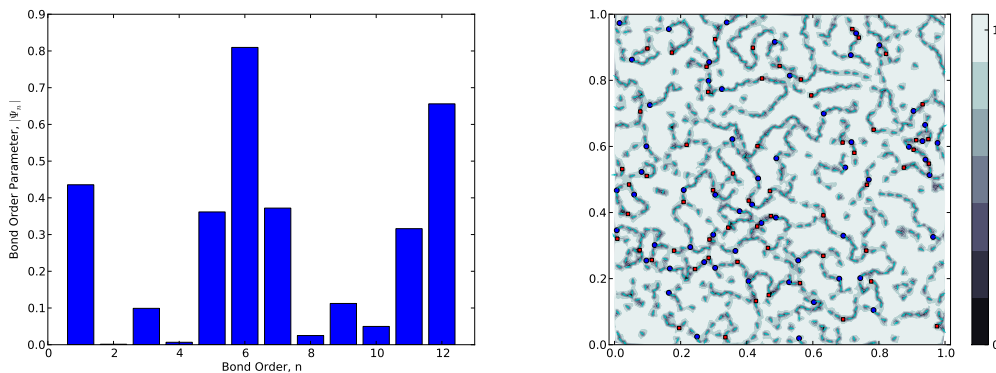


Figure 2.4: Different types of bond-orientational order analysis of the surface pattern shown in Figure 2.3: (a) bar graph of the magnitude of the order parameter  $\Psi_n$ , averaged over all pattern features; for each  $n$  this characterizes the “strength” of patterns with  $n$ -fold symmetry in the image, (b) interpolation of the magnitude of the  $\Psi_6$  order parameter at each pattern feature in the image; this approximates a scalar field that identifies where defects in the 6-fold symmetric or *hexagonal* pattern are located in the image.

In addition to quantification of pattern magnitude, bond-orientational order theory provides information about the orientation of each particle within the pattern. The orientation of pattern feature  $i$  within an  $n$ -fold symmetric pattern is an angle with value  $0 \leq \theta_i \leq \frac{2\pi}{n}$ . This can be computed for each pattern feature, with respect to an arbitrary reference orientation; recalling that  $\Psi_n$  is complex, the orientation is given by its argument

$$\theta_i = \arg \Psi_n. \quad (2.27)$$

As was performed with the bond-orientational order parameter defined at each pattern feature, global and local orientations of the pattern may be computed through averaging and interpolation, respectively. Figure 2.5 shows an example of this for the image in 2.3a.

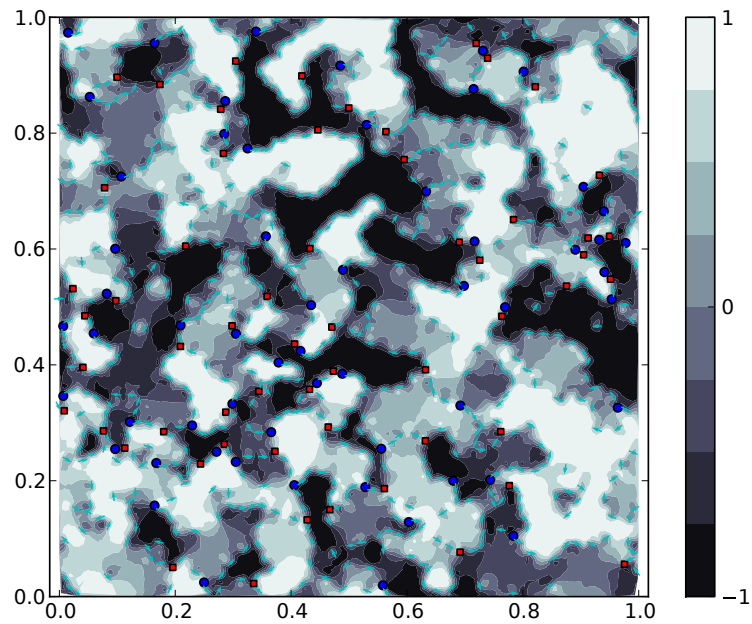


Figure 2.5: Bond-orientational pattern orientation  $\arg \Psi_6$  of the surface pattern shown in Figure 2.3 – interpolation is used to form a continuous field using  $\arg \Psi_6$  values from each of the discrete features. Areas of similar brightness indicate similar hexagonal pattern orientation in the original image.

## Chapter 3

# Theory and Application of Shapelets to the Analysis of Surface Self-assembly Imaging

In this chapter we present a method for identifying pattern scale using spectral density analysis and describing the localized shape at any region within a pattern. This shape characterization is performed using a set of filters known as *shapelets* [15, 16] which, when convolved with the image, give a description of the local behaviour of the pattern. Using steerable filter theory [17] we determine the orientation that maximizes the magnitude of the response of the convolution between the shapelet and the target pattern.

To obtain optimal results we present a method for selecting a subset of shapelets characteristic of the behaviour in a particular pattern using both a qualitative and quantitative approach. Finally, to ensure that the response of each shapelet is maximized for a target pattern, we present a method to select a shapelet's scale parameter,  $\beta$ , to maximize the extracted pattern behaviour. Finally to ensure each shapelet will be optimal for the target pattern we present a method for adjusting a shapelet's scale parameter,  $\beta$ , to match the characteristic length scale of the input pattern. Section 3.2 develops these methods for both selecting the most characteristic subset and optimal size for a given pattern.

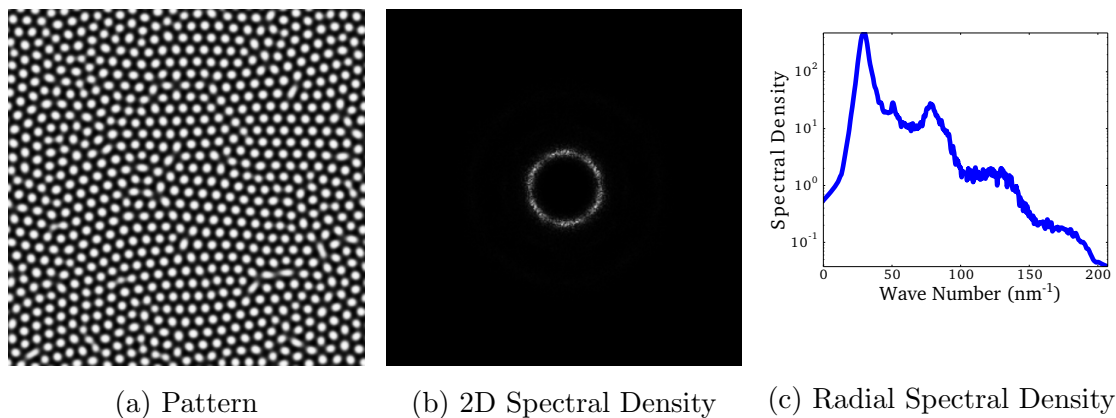


Figure 3.1: Fourier transform: We observe the original pattern in 3.1a with the magnitude of the Fourier Transform in 3.1b. The radial spectral density is shown in 3.1c with LOESS smoothed amplitude over frequencies. Note that although Figure 3.1a is not a pure sinusoid, the sinusoidal components of the figure are highly concentrated in a ring at a frequency of approximately  $27 \text{ nm}^{-1}$ , which is clearly visible in both the 2D spectral density 3.1b and the radially-averaged spectral density 3.1c.

### 3.1 Global Periodic Scale

Any visible pattern requires some form of repetition across the pattern’s domain. This repetition describes the tiling mechanism of the pattern components and can be defined as some scale. Before performing any characterization of a pattern, identifying the scale of repetition allows the pattern to be identified across any scale. As the tiling is performed in some periodic fashion, the scale at which the pattern is repeated is proportional to some discrete frequency.

Identifying this frequency depends on measuring the frequencies contained in an image. Spectral density identifies the characteristic frequencies by evaluating the Fourier transform and examining only the amplitude of each frequency. Figure 3.1 shows a hexagonal pattern with its corresponding spectral density.

Identifying the characteristic wavelength, we remove the effect of frequency direction and only examine the amplitude and wavelength independent of any direction. Analyzing the amplitude for frequencies of a given wavelength, we want to characterize the dominant frequency. This is performed by applying Locally Weighted Scatterplot Smoothing [24] to the wavelength / amplitude function, then finding the peak of this smoothed function gives the dominant wavelength in the pattern. This spectral density plot for the pattern shown

in Figure 3.1 can be observed in Figure 3.1c. After computing the dominant frequency for a given pattern, we can determine the corresponding wavelength and use this value to identify the pattern scale.

## 3.2 Sets of Steerable, Scale-Optimized Shapelets

To use shapelets for pattern analysis, appropriate shapelet sets and optimal scales are first determined based on “prototypical” uniform patterns that approximate real surface self-assembly imaging data, but that have a convenient parametric form. The uniform patterns are expressed in terms of a two-dimensional Fourier series [25],

$$\rho(\mathbf{x}) = \sum_{n=0}^N a_n \exp(i\mathbf{k}_n \cdot \mathbf{x}), \quad (3.1)$$

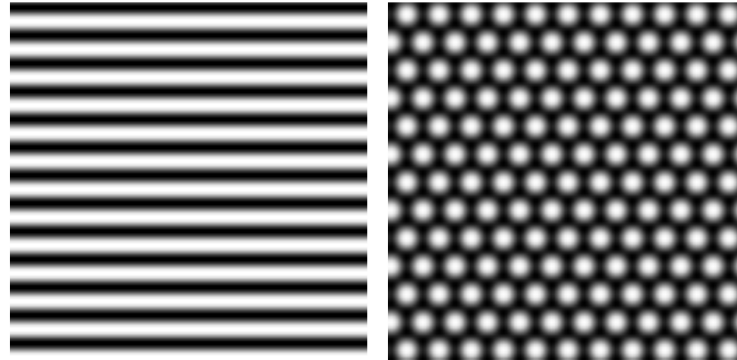
where the constants  $a_n$  are related to the magnitude of the pattern modulation and  $\mathbf{k}_n$  are the basis vectors of the pattern. For one-mode approximations of stripe and hexagonal patterns of interest, the basis vectors are [25],

$$\begin{aligned} \mathbf{k}_1 &= \frac{2\pi}{\lambda} \mathbf{e}_2 \\ \mathbf{k}_2 &= \frac{2\pi}{\lambda} \left( \frac{\sqrt{3}}{2} \mathbf{e}_1 - \frac{1}{2} \mathbf{e}_2 \right) \\ \mathbf{k}_3 &= \frac{2\pi}{\lambda} \left( -\frac{\sqrt{3}}{2} \mathbf{e}_1 - \frac{1}{2} \mathbf{e}_2 \right), \end{aligned} \quad (3.2)$$

where  $\mathbf{e}_1 = (1, 0)^\top$  and  $\mathbf{e}_2 = (0, 1)^\top$ . For a striped pattern,  $a_1 \neq 0, a_2 = a_3 = 0$ , and for a hexagonal pattern  $a_1 = a_2 = a_3 \neq 0$ . The quantity  $2\pi/\lambda$  is the wavenumber for the pattern length scale (wavelength)  $\lambda$ , which corresponds to the peak shown in Figure 3.1c. Using the equation shown in 3.1 we can construct synthetic striped and hexagonal as shown in 3.2a and 3.2b.

In order to select a minimal set of shapelets that respond strongly when applied to uniform stripe and hexagonal patterns, or in general any surface pattern, the sub-set of shapelets should have the following properties:

1. It should contain shapelets with the same fundamental rotational symmetries as the pattern of interest. Stripe patterns have subregions with one- and two-fold symmetry;



(a) Synthetic Stripe:  
 $a_1 = 1, a_2 = 0, a_3 = 0.$

(b) Synthetic Hexagonal:  
 $a_1 = 1, a_2 = 1, a_3 = 1.$

Figure 3.2: Sample Synthetic Patterns generated from Equation 3.1.

hexagonal patterns have subregions with one-, two-, three-, and six-fold symmetry having  $m$  values 1, 2, 3, 6.

2. The response magnitude of the shapelets should be *invariant* with respect to rotations of the pattern.
3. The shapelets should respond most strongly to the dominant pattern frequencies.

### 3.2.1 Pattern Symmetries

From Figure 2.2, a convenient property of shapelets of order  $(m, n)$  with  $n = 0$  and  $m > 0$  is that they have  $s$ -fold rotational symmetries for  $s$  corresponding to all divisors of  $m$ . This symmetry describes what rotations of an object results no visible change. For instance, a square centred at the origin is considered to have four-fold symmetry as any rotation of  $90^\circ$  results in no observable rotation.

This same level of symmetry can be considered for patterns. As a perfect striped pattern rotated  $180^\circ$  forms a striped pattern of the same orientation, shapelets up to order  $m = 2$  are necessary to describe the pattern. Hexagonal patterns have a six-fold symmetry and therefore require shapelets up to order  $m = 6$  to describe them. An important observation is that using shapelets of an order greater than the pattern does not negatively impact the decomposition. As defective regions contain behaviour not characteristic of the pattern, they must contain some behaviour of a different symmetric behaviour. Extracting this

behaviour of a higher degree of symmetry can extract metrics capable of measuring this behaviour and produce a higher likelihood of detecting a defective region.

### 3.2.2 Rotational Invariance

Analyzing a pattern independent of its orientation requires each shapelet response remain constant under rotation. Such a response would orient the shapelet to provide a response at its optimal orientation as shown in Figure 3.3c. One option for obtaining this optimal orientation is to convolve the image with multiple rotations of the same image while searching for an optimal rotation at each location. As each location may possess a different optimal orientation, this search would need to be performed linearly over the set of orientations. An important note is that while it would technically be possible to perform some form of convex search at each location, the convolution would require a differently oriented filter at each location and would therefore take  $O(n^4)$ .

These approaches have two major drawbacks: (i) the large number of shapelet responses that would need to be evaluated for each orientation and pixel (ii) the optimal orientation provided would be an estimation and not an exact value.

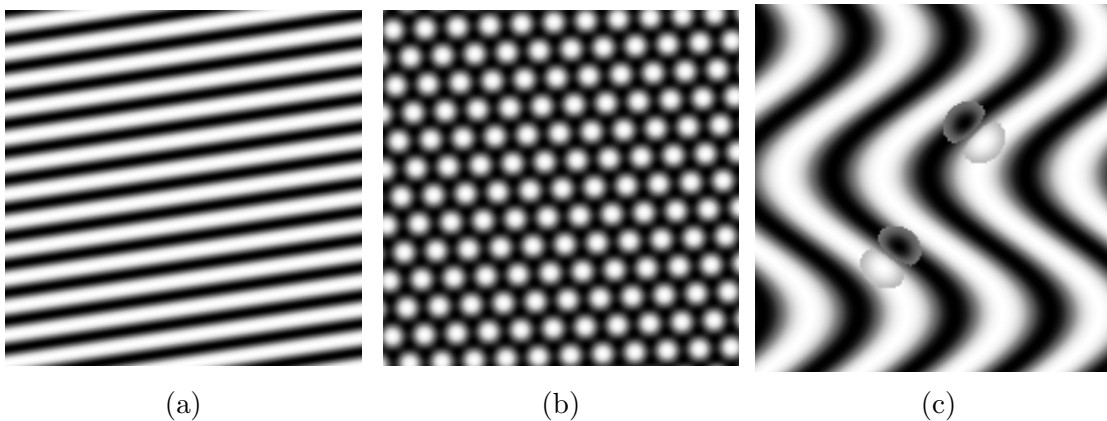


Figure 3.3: Plots of one-mode approximations of a (a) striped and (b) hexagonal pattern generated from Eqns. (3.1)–(3.2) and rotated; (c) Schematic of rotations of a shapelet applied to a nonuniform striped pattern.

Rather than solve for the optimal rotation approximately, an exact solution is derived from the fact that the shapelets are steerable.

**Lemma 1.** Let  $B_{n,m}(x, y; \beta, \varphi) = B_{n,m}(x \cos \varphi - y \sin \varphi, x \sin \varphi + y \cos \varphi; \beta)$  be a shapelet as defined in Equation (2.25) that has been rotated clockwise through a phase angle  $\varphi$  as described in Section 2.2.3. Then,

$$\Re[B_{n,m}(x, y; \beta, \varphi)] = \cos(m\varphi) \Re[B_{n,m}(x, y; \beta)] + \sin(m\varphi) \Im[B_{n,m}(x, y; \beta)]. \quad (3.3)$$

The full proof is shown in A.1.1.

**Lemma 2.** Let  $w_{0,i} = f \star B_{0,i}(\cdot, \cdot; \beta)$ , and define  $\varphi_{0,i}^* = \arg \max_{\varphi} \Re[f \star B_{0,i}(\cdot, \cdot; \beta, \varphi)]$  and  $w_{0,i}^* = \Re[f \star B_{0,i}(\cdot, \cdot; \beta, \varphi_{0,i}^*)]$ . Then,

$$\varphi_{0,i}^* = \arg w_{0,i}, \quad w_{0,i}^* = |w_{0,i}|. \quad (3.4)$$

The full proof is shown in A.1.2.

Here,  $\varphi_{0,i}^*$  is the shapelet orientation at which the real part of the *steered* shapelet response is maximal and  $w_{0,i}^*$  is the value of the response at that orientation. In the above, the dependence of  $\varphi_{0,i}^*$  and  $w_{0,i}^*$  on  $x$ ,  $y$ , and  $\beta$  is suppressed in the notation for clarity, but the lemma immediately applies to translated and scaled versions of shapelets as well. As desired, the rotation-optimized response  $w_{0,i}^*$  is invariant to rotations of the pattern.

### 3.2.3 Scaling

The scale of a shapelet,  $\beta$ , affects the shapelet response. Selecting a scale that maximizes the shapelet response ensures that it responds strongly to the pattern behaviour and does *not* respond strongly to pattern defects. Finding this  $\beta$  parameter for a particular pattern is dependent on the pattern behaviour and is proportional to scale of the pattern. Therefore if the image is downsampled by a factor of two, the  $\beta$  will be decreased by the same factor. As the pattern scale can be determined using spectral density methods as shown in Section 3.1 the  $\beta$  parameter can be varied for patterns of different scale using characteristic wavelength. Determining this relationship for a fixed pattern, we evaluate the function below given the pattern, location  $(x, y)$ , and optimal orientation  $\varphi^*$  of a shapelet, to measure the shapelet response given by the correlation of the shapelet with the image function  $f$ ,

$$w_{n,m}^*(\beta) = f \star \Re[B_{n,m}(\cdot, \cdot; \beta, \varphi^*)] \triangleq \sum_{x'} \sum_{y'} f(x', y') \Re[B_{n,m}(x', y'; \beta, \varphi^*)], \quad (3.5)$$

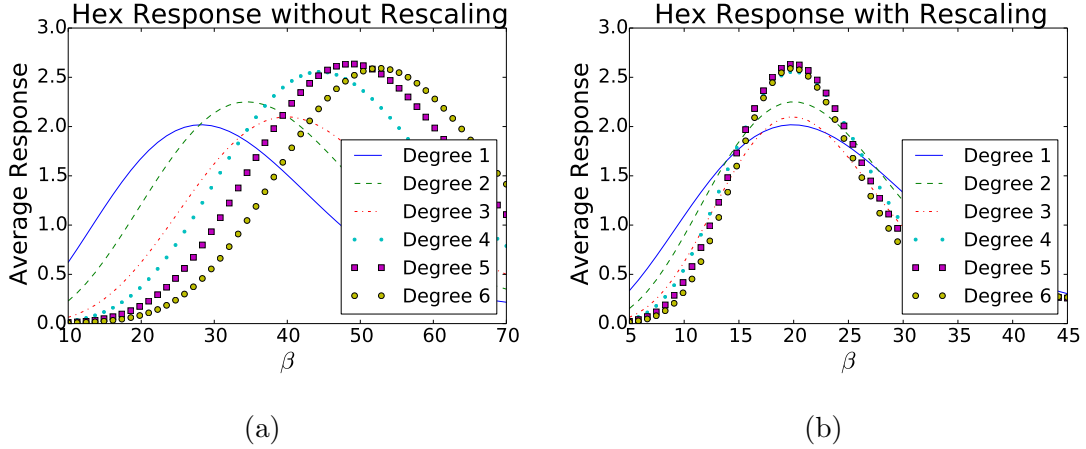


Figure 3.4: Shapelet filter response versus  $\beta$  (a) before and (b) after rescaling of  $\beta$  with respect to  $\lambda$ . Responses shown are correlations with the uniform pattern given by Eqns. (3.1)–(3.2). The vertical axis was obtained using (3.6)

the value of  $\beta$  can be varied to find the optimal value for the given image function; an example for different  $(n, m)$  is shown in Figure 3.4.

$$\max_{\beta} \sum_{x,y} \|(S_{m,n}^{\beta} \star F)[x, y]\| \quad (3.6)$$

To ensure that chosen shapelets respond optimally to the target pattern of interest,  $\beta$  is chosen to maximize the  $w_{S_{m,n}^{\beta}}^*$  throughout the image response as shown in Eq. (3.6). For a given pattern length scale  $\lambda$ , the maximal shapelet response was found to *not* be at  $\beta = \lambda$ , but rather at  $\beta = C\lambda$ , with  $C$  depending on the shapelet type and pattern behaviour. Appropriate constants  $C$  were found for each shapelet using grid search on  $R$ ; these are given in Table 3.1 and was used for all subsequent analysis.

Figure 3.5 shows local pattern response values resulting from application of the scale-optimized steerable shapelets to uniform (i) stripe and (ii) hexagonal patterns using the uniform pattern given by Equation (3.1). The shapelet responses shown in Figure 3.5a and Figure 3.5b reveal the locations in the pattern that have different rotational symmetries. For example, the  $m = 1$  shapelet applied to the striped pattern reveals where the pattern has only 1-fold symmetry: this occurs at the boundaries between stripes. At such locations,

Table 3.1: Coefficient values for  $\beta = C\lambda$  for shapelets up to order six.

$(\mathbf{m}, \mathbf{n})$	$C$	$(\mathbf{m}, \mathbf{n})$	$C$
(1,0)	1.418	(2,0)	1.725
(3,0)	2.003	(4,0)	2.224
(5,0)	2.439	(6,0)	2.640

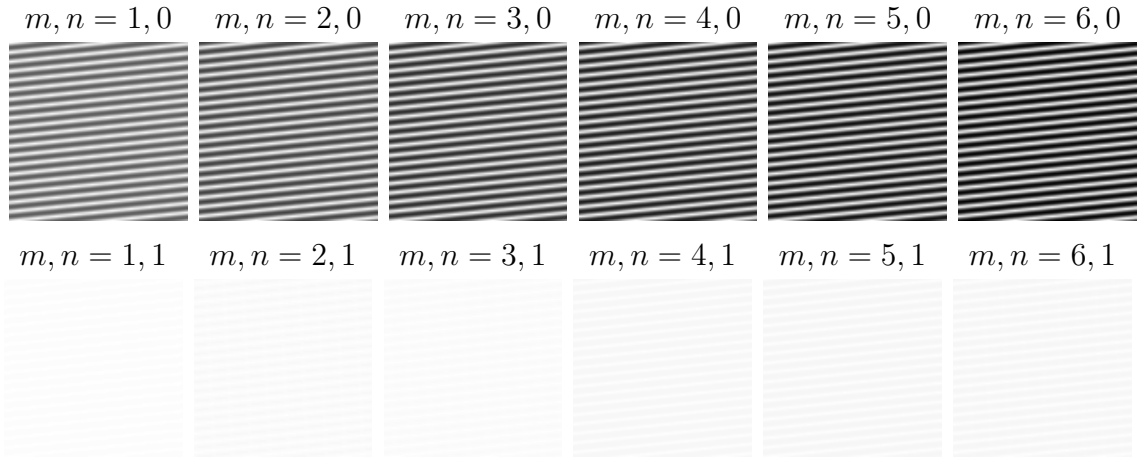
the pattern is only self-similar when rotated by  $2\pi$ . On the other hand, the  $m = 2$  shapelet responds at peaks and troughs in the striped pattern, where a  $\pi$  rotation results in a self-similar pattern. As the shapelet order is increased beyond  $m = 2$ , almost no new local pattern information is extracted; the rotation-optimized responses of the shapelets with higher-order symmetry are very similar to the  $m = 1$  or  $m = 2$  case.

The  $m = 1$  response applied to the hexagonal pattern responds at locations near the “edge” of a pattern mode, which have only one-fold symmetry. The  $m = 2$  and  $m = 4$  shapelets respond strongly to areas that are midway along a line joining two pattern modes; these locations have two-fold symmetry. The  $m = 3$  shapelet responds very strongly to the three-fold symmetry at “saddle points”—that is, at points in the pattern that are equidistant from three nearby modes, and finally the  $m = 6$  shapelet responds strongly at pattern modes where there is six-fold rotational symmetry. Note that the hexagonal pattern lacks any two-fold symmetry; thus the  $m = 5$  shapelet, which has only five-fold and one-fold symmetry responds only at pattern locations with one-fold symmetry which are also identified by the  $m = 1$  shapelet.

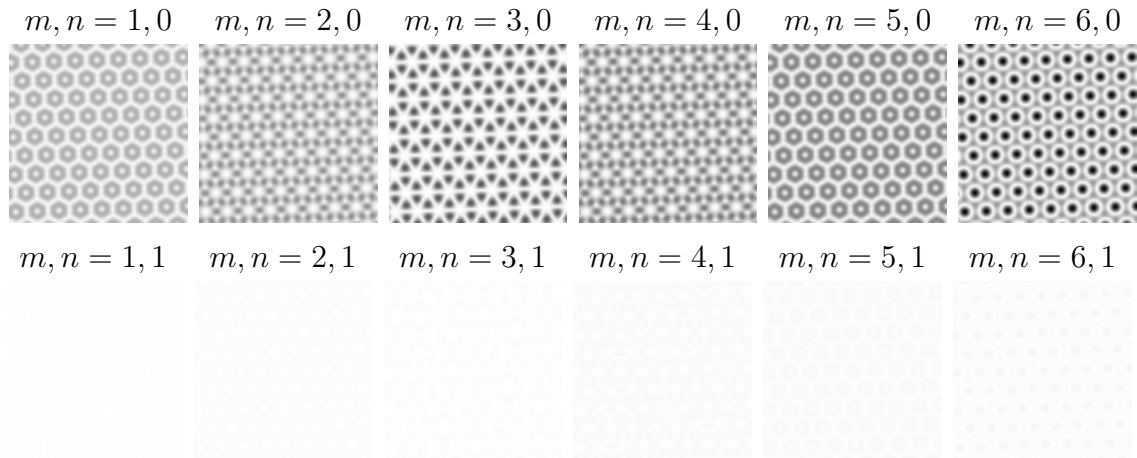
The next section explains how the responses of different shapelets can be combined into a useful quantitative analysis of the underlying image.

### 3.3 Application to Self-Assembly Imaging

Surface self-assembly imaging typically involves surfaces with patterns that are non-uniform and pattern features that are not well-approximated using a one-mode assumption. Figures 3.6 and 3.7 show two examples images of two-dimensional surface self-assembly where non-uniform stripe and hexagonal patterns are present (taken from [13]). In Figure 3.6 the pattern features themselves vary in shape as is shown in Figure 3.6. In Figures 3.7a-3.7d multiple quasi-uniform subdomains, or “grains”, are present with defect regions (grain boundaries) at the interface between them. In order to test the presented shapelet-based method on these realistic patterns, a guided machine learning approach was used to classify regions with uniform patterns from those with defects.



(a) Responses to striped pattern



(b) Responses to hexagonal pattern

Figure 3.5: Responses of steerable polar shapelet filters applied to uniform one-mode approximations of a (a) striped and (b) hexagonal pattern from Eqns. (3.1)-(3.2). Both (a) and (b) have the responses normalized between filters visualized with increasing darkness representing increasing magnitude of response.

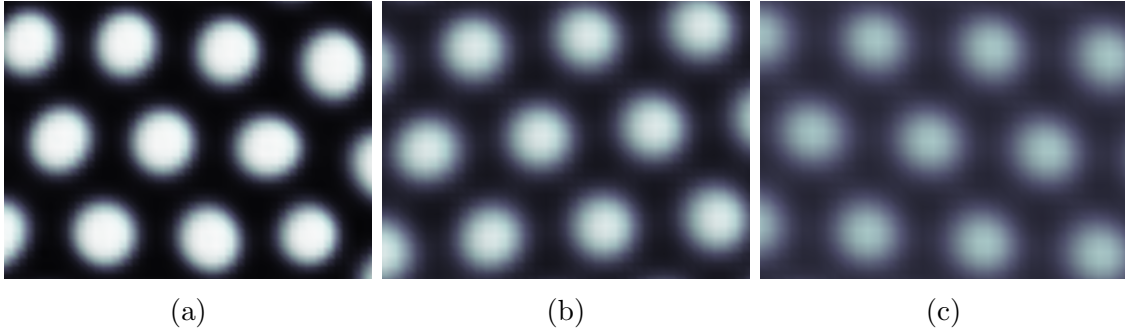


Figure 3.6: Examples of hexagonal surface self-assembly with features of varying character: (a) sharp interface, (b) semi-diffuse interface, (c) diffuse interface. Figures taken from ref. [13]

The *response space* is defined as  $\mathbf{r} \in \mathbb{R}^p$  where  $p$  is the number of steerable shapelet filters used to quantify the pattern. Thus at each point in the image  $(x, y)$ , a response vector  $\mathbf{r}$  is computed,

$$\mathbf{r}(x, y) = \frac{[w_{0,1}^*(x, y), w_{0,2}^*(x, y), \dots, w_{0,p}^*(x, y)]^\top}{\|[w_{0,1}^*(x, y), w_{0,2}^*(x, y), \dots, w_{0,p}^*(x, y)]\|_2} \quad (3.7)$$

consisting of the shapelet responses  $w_{0,j}^*(x, y)$  under the optimal orientation for image location  $(x, y)$  from Eqn. (3.4). Given a user-specified set of coordinate pairs (i.e. pixel locations)  $\mathcal{R}$  of a defect-free subdomain of the image, at any location of interest  $(x', y')$  in the image the *response distance* may be defined from the pixel  $(x', y')$  to the reference set.

$$d_{\mathbf{r}}((x', y'), \mathcal{R}) = \min_{(x, y) \in \mathcal{R}} \|\mathbf{r}(x', y') - \mathbf{r}(x, y)\|_2, \quad (3.8)$$

where  $d_{\mathbf{r}}((x', y'), \mathcal{R})$  is the Euclidean distance between the response vector at the location of interest and the closest response vector in the reference set.

The response distance encapsulates how different the image is at location  $(x', y')$  from the reference set in terms of the relative shapelet responses. It serves to highlight areas in the image where defects are present or where no pattern is present. Such areas have response vectors that have larger  $d_{\mathbf{r}}((x', y'), \mathcal{R})$  from those where no defects are present.

This application of the steerable shapelets method was applied to the striped and hexagonal self-assembled domain images shown in Figure 3.7. The characteristic pattern wavelength  $\lambda$  found through the maximum peak of the spectral density (inset of Figure 3.7) was used to determine the appropriate shapelet scale factors as described in Section

3.2. Figures 3.7b-3.7e illustrate the normalized Euclidean distance of the response vectors at each pixel with respect to the response vector of the uniform domain shown in Figure 3.7. In this figure, intensity is inversely proportional to  $d_r(\cdot, \mathcal{R})$  for the given quasi-uniform reference set, which clearly reveals the locations of defects in the image. Note that response distance is *invariant* to pattern rotations, because the elements of the response vectors are invariant to pattern rotations.

Pattern defects generally fall into two types: translational and orientational and are referred respectively as dislocation and disclination defects [26] as shown in Figure 3.7. In striped patterns, dislocations correspond to regions where a striped feature begins (+) or ends (-). In hexagonal patterns, dislocations correspond to the beginning (+) or end (-) of a row of hexagonal features. Orientational defects and disclinations are manifested in a rapid transition from one pattern orientation to another. In striped patterns, the majority of disclinations involve a  $\frac{\pi}{2}$  rotation and in hexagonal patterns, they involve a  $\frac{\pi}{6}$  rotation.

The steerable shapelets method results, shown in Figure 3.7, show a direct relation between areas of strong response and quasi-uniform areas in the original pattern images. Areas where response is minimal corresponds to one of three localized cases: (i) the presence of defects, (ii) large strain of the pattern (stripe curvature and or dilation/compression), (iii) deviation of the pattern feature from the one-mode approximation.

With respect to defects present in both images, the image analysis results show good agreement with visual inspection of local topology in the original image. In areas of large strain of the pattern, which are typically also in the locality of defects, the shapelet response decays smoothly. This could be considered a drawback in that the method does not strongly distinguish between defect “core” regions and the region of strain surrounding the core. Alternatively, resolving the entirety of the region influenced by a single defect, or cluster of defects, likely has a significant impact in relating pattern quality to material properties. Finally, in both images there are pattern features that strongly deviate from the one-mode approximation of the pattern. In the striped pattern there are regions with convex circular shape and in the hexagonal pattern there are regions with lamellar-like features. The method is both robust in the presence of these features and strongly responds to their presence.

## 3.4 Conclusions

A method for quantitative analysis of surface self-assembly imaging was presented and applied to images of stripe and hexagonal ordered domains. A set of orthogonal functions,

shapelets, were shown to be useful as filters which respond optimally to surface patterns with  $n$ -fold symmetry where  $n$  is the order of the shapelet. Steerable formulations of the shapelet functions were derived using steerable filter theory and used to efficiently compute the filter rotation which yields maximal response. The utility of the steerable shapelet filter approach was demonstrated on uniform stripe and hexagonal patterns. Furthermore, realistic nonuniform surface patterns were analyzed using the presented steerable shapelet method through guided machine learning. This approach is able to *quantitatively* distinguish between uniform (defect-free) and non-uniform (strained, defects) regions within the imaged self-assembled domains. The presented method is both computationally efficient, requiring only two shapelet evaluations per steerable shapelet, and robust in the presence of variation in pattern feature shape. Finally, the shapelet-based method provides a significantly increased granularity value compared to the bond-orientational order method (feature-level).

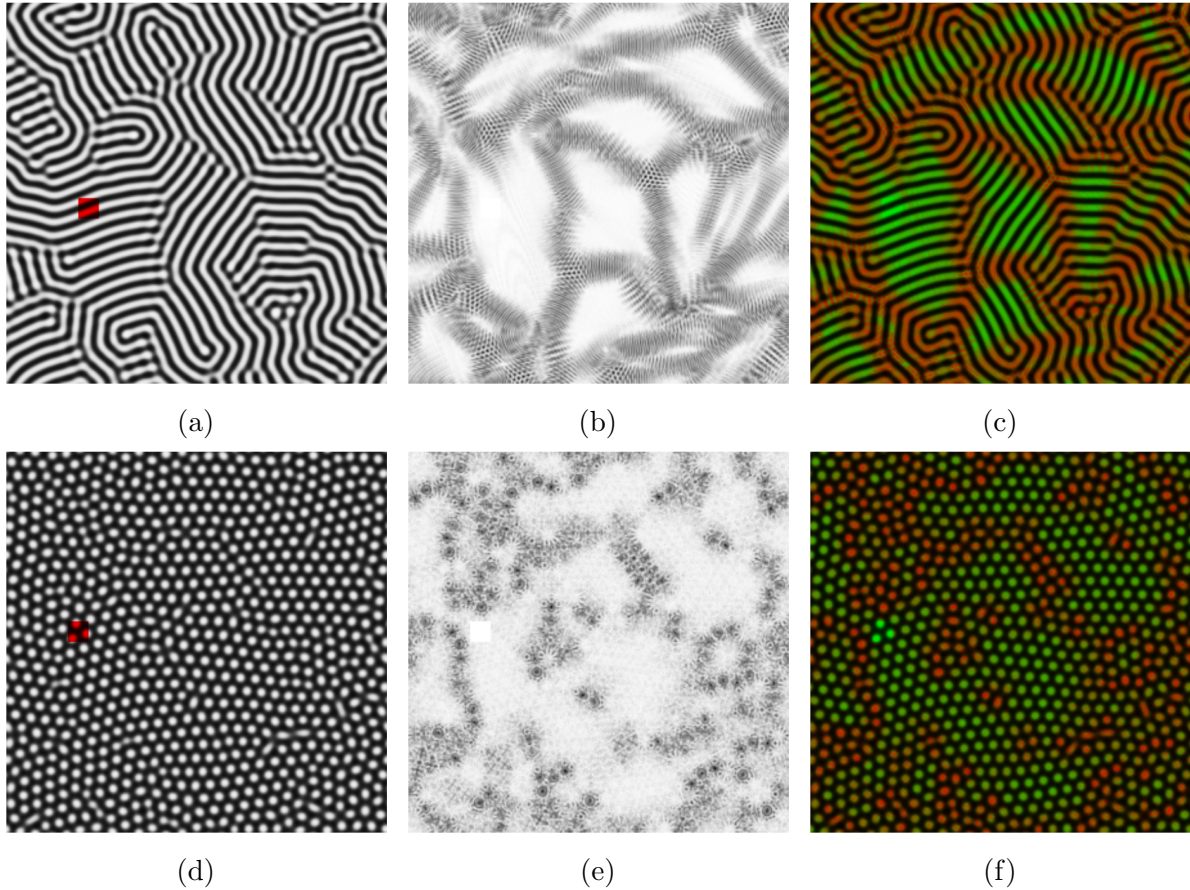


Figure 3.7: Examples of non-uniform (a) striped and (d) hexagonal patterns from simulations of surface self-assembly (taken from ref. [13]) with inset spectral density plots; Results from applying the guided machine learning algorithm to the (b) stripe and (e) hexagonal patterns where the response distance (Eqn. (3.8)) was normalized to range from 0 (black) to 1 (white) and the user-specified set of pixels are highlighted in (a,d). This information is overlaid in c and f with red indicating defects and green being well formed. Additional samples can be found in Appendix A.2.

# Chapter 4

## Improved Analysis using Orientation Extraction

In the previous chapter, we demonstrated that combining shapelet analysis and steerable filter theory yields a computationally efficient technique for the analysis of regular patterns. In particular, we demonstrated the ability to distinguish regions of pattern uniformity and regions where defects are present. We analyzed a set of non-uniform surface self-assembly images and using supervised machine learning, we measured the similarity between different regions by comparing their local behaviour, which was expressed in terms of shapelet responses. To accomplish the analysis we used the *magnitudes* of each steerable shapelet response, but the *orientation* of the maximal response is not used for any of the shapelets. As this orientation information was missing from the classification this resulted in a divergence from measuring squared error of the image and the shapelet error measurement.

In this chapter, we develop an analogous but enhanced analysis method that evaluates similarity of two image regions based on both the magnitude *and* orientation values produced by the shapelets at each location. We apply our method to non-uniform hexagonal and striped imaging of self-assembled surfaces, and we find that it provides a more accurate pattern and defect classification while also providing an estimate of the local pattern orientation at each point. The computational cost of the method is higher than the magnitude-only method; we expect that the choice of method for any particular application will involve a trade-off between the richness of the desired output and computational demands and resources.

## 4.1 Comparison of Sets of Steerable Shapelet Filter Responses

As shown in the previous chapter, the application of sets of steerable shapelets up to  $m$ -fold symmetry yields both a response magnitude  $w_{n,m}^*$  and filter orientation corresponding to the maximal response  $\varphi_{n,m}^*$ . Because in practice we use only shapelets for which  $n = 1$ , from here on we will use a condensed notation for these values  $w_m^x$  and  $\varphi_m^x$  for a shapelet of  $m$ -fold symmetry from image  $x$ . From Figures 4.1a and 4.1d, we apply the set of filters to two different sub-regions in the image and yield a vector for each filter composed of  $w_m$ , its magnitude, and  $\varphi_m$ , its orientation.

In the previous chapter, the output of our shapelets was used as a measurement or summary of the patterns in our image at a particular point by describing the most prominent local behaviour. However, we can also take a *synthetic* or *generative* view of the output of the shapelets: As the shapelets were designed to form an orthonormal basis, the set of magnitudes and orientations at a particular point, together with the shapelet definitions themselves, can be used to reconstruct the localized regions when projected onto our shapelet filter space. Given an image function  $F$ , we form a reconstruction  $\hat{F}$  using a set of shapelets  $S_m^{\beta_m}$  with  $w_m$  and  $\varphi_m$  obtained from (3.5) and (3.4).

$$\hat{F} = \sum_m w_m S_m^{\beta_m}(x, y; \varphi_m) \quad (4.1)$$

which uses the magnitude  $w_m$  and angle  $\varphi_m$  of the filter response, with its corresponding shapelet  $S_m^{\beta_m}$ , to create the estimate of local behaviour. Figures 4.1b, 4.1c, 4.1e and 4.1f show the reconstructed estimator when created with the appropriate responses and rotation. The reconstruction essentially removes all content in the region that cannot be represented by our set of shapelets, but preserves periodic behaviour up to order  $m$ .

We define the (inverse) similarity between two arbitrary regions in our image by the minimal squared error between their respective shapelet-based reconstructions if we allow one of the reconstructions to rotate by an angle  $\theta$ . This is analogous to the method presented in Chapter 2, but requires that we rotate *all shapelets simultaneously by the same angle* rather than rotating each shapelet independently, preserving the relative orientation between the sets of shapelets.

From Figure 4.1, we can see that reconstructions (b) and (c) would be most similar (i.e. have small distances) if (c) were to be rotated by approximately  $\pi$  radians. Similarly, reconstructions (e) and (f) would be closest if (f) were to be rotated by approximately  $\pi/3$  radians. This alters the definition of orientation to being described in terms of the difference of orientation between component shapelets.

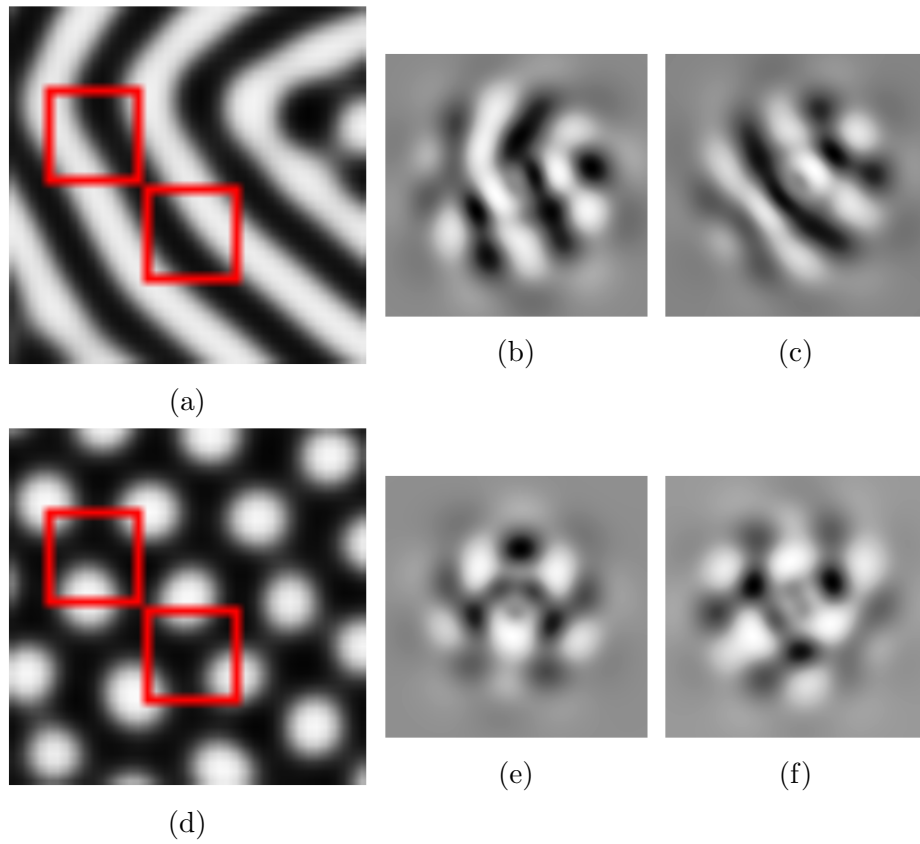


Figure 4.1: Localized reconstructions of two hexagonal pattern regions indicated in 4.1a are shown in in 4.1b and 4.1c. This process is repeated for a striped pattern with regions shown in 4.1d with reconstructions in 4.1e and 4.1f.

## 4.2 Orientation-Enhanced Comparison of Sets of Steerable Shapelets

First, we note that if we do not allow our reconstructions to rotate we may express the squared error between reconstructions<sup>1</sup> at locations  $f$  and  $g$ , as follow:

$$\text{Err}^\perp(\hat{F}, \hat{G}) = \left| \hat{F} - \hat{G} \right|^2 = \left| \sum_m \left( w_m^f S_m^{\varphi_m^f} - w_m^g S_m^{\varphi_m^g} \right) \right|^2 \quad (4.2)$$

$$= |w^f|^2 + |w^g|^2 - 2 \sum_m \left( w_m^f w_m^g \left( S_m^{\varphi_m^f} \cdot S_m^{\varphi_m^g} \right) \right). \quad (4.3)$$

Equation 4.3 follows from 4.2 by the mutual orthogonality of the shapelets; therefore computing the error between  $\hat{F}$  and  $\hat{G}$  can be reduced to computing the correlation between the reconstructions. As these reconstructions are created from a set of orthonormal filters, this in turn reduces to evaluating the correlation between each component of the respective reconstructions. This approach reduces computing squared error to computing the correlation of each shapelet's response in both  $F$  and  $G$ .

Allowing one of the reconstructions to rotate by  $\theta$ , we consider the effects on the measured error. Without loss of generality, we consider rotating the second reconstruction to minimize our error function:

$$\text{Err}(\hat{F}, \hat{G}) = \min_{\theta \in [0, 2\pi)} \left[ |w^f|^2 + |w^g|^2 - 2 \sum_m \left( w_m^f w_m^g \left( S_m^{\varphi_m^f} \cdot S_m^{\varphi_m^g + m\theta} \right) \right) \right] \quad (4.4)$$

Recovering the optimum  $\theta$ , also gives a measurement of the relative orientation between the two patterns. Finding the optimum rotation to the estimators shown in Figure 4.1, we can optimally rotate  $F$  with respect to  $G$  as shown in Figure 4.2.

Examining the minimization problem in Equation 4.4, we observe that it is equivalent to maximizing the weighted sum of correlations between the shapelets that make up  $\hat{F}$  and  $\hat{G}$ . Each correlation is taken between two shapelets with the same symmetry  $m$  but different rotation which forms a simple function as follows

$$S_m^{\varphi_m^f} \cdot S_m^{\varphi_m^g} = \cos(\varphi_m^f - \varphi_m^g). \quad (4.5)$$

---

<sup>1</sup>Recall that when we write  $|F - G|^2$  for two images (reconstructions or "originals") we refer to the sum over pixel locations of the squared intensity differences.

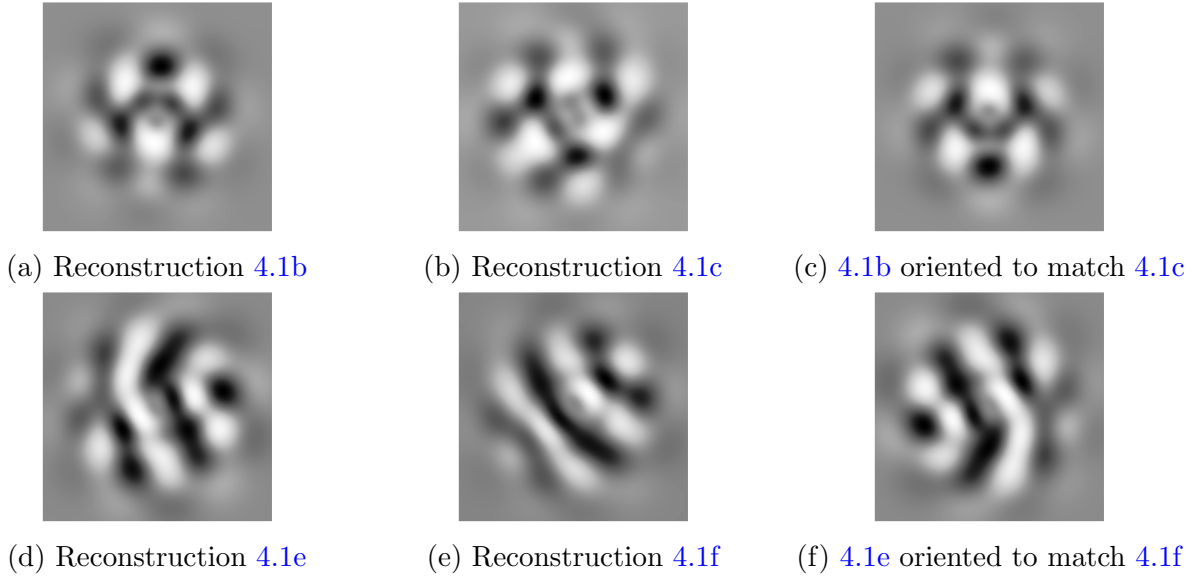


Figure 4.2: Optimal rotated reconstructions. The same reconstructions from Figure 4.1 are shown with 4.2b and 4.2e optimally rotated to match 4.2c and 4.2f, respectively. (Note that the second and third column match better than the first and second column.)

This allows us to simplify Equation 4.4 to

$$\text{Err}(\hat{F}, \hat{G}) = |w^f|^2 + |w^g|^2 - 2 \max_{\theta} \left[ \sum_m (w_m^f w_m^g \cos(\varphi_m^f - (\varphi_m^g + m\theta))) \right]. \quad (4.6)$$

Simplifying the summation we combine the magnitude and orientation components into the grouped values  $w_m$  and  $\varphi_m$ .

$$w_m = w_m^f w_m^g \quad (4.7)$$

$$\varphi_m = \varphi_m^f - \varphi_m^g \quad (4.8)$$

$$\begin{aligned} \text{Err}(\hat{F}, \hat{G}) &= |w^f|^2 + |w^g|^2 - 2 \max_{\theta} \sum_m w_m \cos(\varphi_m - m\theta) \quad (4.9) \\ &= |w^f|^2 + |w^g|^2 - 2 \max_{\theta} \sum_m [w_m \cos(\varphi_m^g) \cos(m\theta) + w_m \sin(\varphi_m^g) \sin(m\theta)]. \end{aligned} \quad (4.10)$$

Using this new form we can make a number of observations about comparing reconstructions using the magnitude and orientation of shapelet functions. As shapelets oscillation under rotation occur at discrete frequencies and the correlation between two shapelets of the same type and differing orientation is sinusoidal, the different orientation between the two shapelets acts as a phase shift in the error function. With the magnitude component weighting the correlation measurement, it can be interpreted as a phase shift component. This same form can be observed in the real components of the DFT as shown below:

$$\mathcal{F} \left\{ \vec{X} \right\} = \sum_n^N x_n e^{-i2\pi kn/N} \quad k \in \mathbb{Z} \quad (4.11)$$

$$= \sum_n^N x_n \cos(2\pi kn/N) - x_n i \sin(2\pi kn/N) \quad (4.12)$$

$$\mathbb{R} \left\{ \mathcal{F} \left\{ \vec{X} \right\} \right\} = \sum_n^N \mathbb{R}\{x_n\} \cos(2\pi kn/N) + \mathbb{I}\{x_n\} \sin(2\pi kn/N) \quad (4.13)$$

$$x_n = a_n \cos(\varphi_n) + i a_n \sin(\varphi_n) \quad (4.14)$$

$$\mathbb{R} \left\{ \mathcal{F} \left\{ \vec{X} \right\} \right\} = \sum_n^N a_n \cos(\varphi_n) \cos(2\pi kn/N) + a_n \sin(\varphi_n) \sin(2\pi kn/N). \quad (4.15)$$

Using this new observation we can solve for the optimal orientation by evaluating the Fourier transform using the magnitude and orientation components of the shapelet responses as the Fourier coefficients while providing research in Fourier theory to more efficiently optimize the orientational measurement.

### 4.2.1 Application to Self-Assembly Imaging

Using the improved correlation metric 4.6, we processed sample striped and hexagonal surface self-assembly images shown in Figures 3.7a–3.7d. Results include pattern response and orientation are shown in Figures 4.4a and 4.3a. Comparing results with the previous method, which only provides pattern response shown in Figures 3.7b–3.7e in the previous chapter, the new method also shows a direct relation between areas of strong response and quasi-uniform areas in the original pattern images. As with the previous method, areas where response is minimal corresponds to one of three localized cases: (i) the presence of defects, (ii) large strain of the pattern (stripe curvature and or dilation/compression) and

(iii) deviation of the pattern feature from the one-mode approximation. The new rotational invariant method is evaluated with respect to the nearest neighbour method of Chapter 3 within these three cases.

Pattern response in the vicinity of defects in the pattern, once again, correspond with the visual defects of local topology in the original image. Comparing the pattern response of the previous rotationally agnostic method with the new orientationally sensitive method, this new method shows a more desirable abrupt decrease in response as a defect region is approached. This is compared to a gradual and oscillatory decay in response from the old method, which may now be understood as numerical artifacts resulting from incorrect orientation of the sample domain with respect to the reference domain. The undesirable decay of the shapelet response in areas of significant pattern rotation observed in the old method are completely absent in the new one. Thus the new method distinguishes between defect “core” regions and the region of strain surrounding the core.

Information in regions of strain in the pattern where there is significant mismatch between the orientation of different regions is not lost in this new method. It is instead quantified in the pattern orientation field data, shown in Figures 4.4b and 4.3b. Orientation is observed to be constant in different sub-regions of the pattern, which may be verified from visual inspection of the striped and hexagonal pattern images. There are many areas where the computed orientation varies rapidly which may be directly related to defect regions in the original image. In these defective regions, pattern orientation is not well-defined, which implies that the orientation data is coupled to the pattern response data.

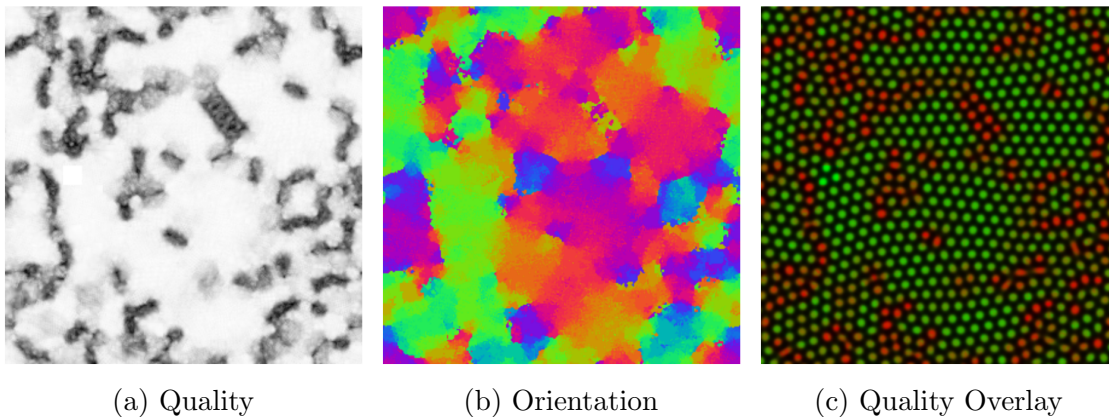


Figure 4.3: Applying the new approach to the hexagonal pattern in 3.7d we obtain a measurement of material quality in 4.3a. The orientation value  $\theta$  is shown in 4.3b using a color with the value  $(R, G, B) = (\sin(\theta), \sin(\theta + 2\pi/3), \sin(\theta + 4\pi/3))$ .

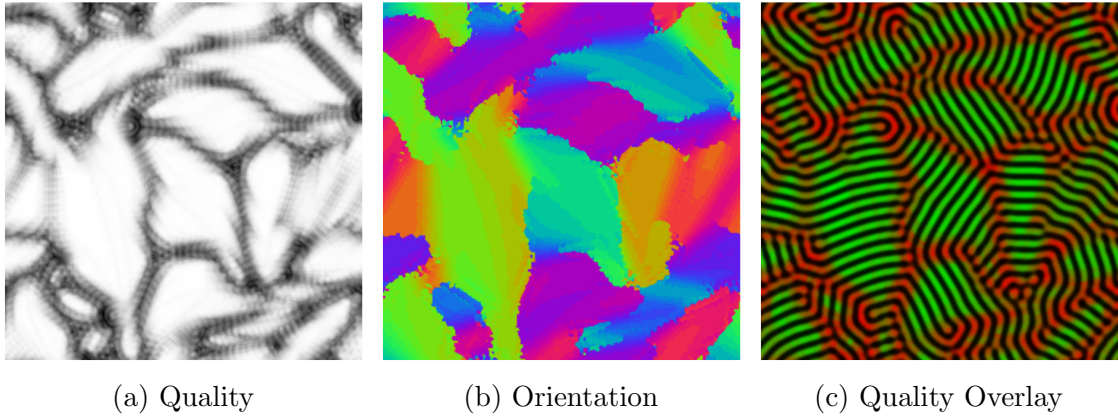


Figure 4.4: Applying the new approach to the striped pattern in 3.7a we obtain a measurement of material quality in 4.4a. The orientation value  $\theta$  is shown in 4.3b using a color with the value  $(R, G, B) = (\sin(\theta), \sin(\theta + 2\pi/3), \sin(\theta + 4\pi/3))$ .

### 4.3 Conclusions

An improved method for quantitative analysis of surface self-assembly imaging was presented and applied to images of striped and hexagonal ordered domains. This method consistently integrated pattern response and orientation information from sets of steerable shapelet filters in a rotation-invariant way. Inclusion of this rotation invariance in the improved guided machine-learning method was shown to enable distinction of regions with pattern defects from those with high degrees of pattern strain. Furthermore with the inclusion of orientation data in the classification we obtain a new pattern metric, local orientation, along with a significantly enhanced method for detecting the presence of both uniform and defective pattern regions using a robust and unified approach.

# Chapter 5

## Conclusions

### 5.1 Conclusions

A method for quantitative analysis of surface self-assembly imaging was developed and shown to enable a unified approach for differing surface patterns (striped and hexagonal). This method is based on:

1. A set of orthogonal functions, shapelets, which were reformulated to be steerable using steerable filter theory and used to efficiently compute the filter rotation, which yields maximal response.
2. A guided machine learning method for rotationally invariant comparison of the shapelets projections within a sample image of a surface self-assembly domain.

This approach was shown to *quantitatively* distinguish between uniform (defect-free) and non-uniform (strained, defects) regions and provide local pattern orientation robustly in the presence of degenerate areas (defects). The presented method is both computationally efficient and robust in the presence of variation in pattern feature shape. Finally, the method provides significantly enhanced resolution (pixel-level) compared to existing methods such as the bond-orientational order method (feature-level).

### 5.2 Recommendations

1. **Image Coarsening** – Depending on the scale of the pattern, the size of reference pattern stored for performing the nearest neighbours comparison could be substan-

tially reduced. To reduce the computational complexity, reducing the size of the reference pattern could be achieved by storing only “unique” points in the reference pattern; that is, by removing points from the reference pattern that have redundant information.

2. **Image Interpolation** – If we assume (or determine) that image data is smooth, changing the model from a discrete pixel-based representation to a continuous  $N$ -dimensional filter space representation could provide a more accurate model of the pattern instead of the existing point-based approach. This can be performed by modelling the shapelets magnitudes as a manifold instead of a set of  $n$ -dimensional points (where  $n$  is the number of shapelets).
3. **Eigen Shapelets** – During filter selection we also propose the introduction of Eigenvector-based filters. Rather than selecting raw polar shapelets, it is possible to produce hybrid shapelets using PCA from their response with a sample image. As long as only shapelets of the same rotational complexity are combined, the steerable property holds true. Using these Eigen-shapelets we could substantially improve the performance and better characterize the pattern while requiring significantly fewer filters.
4. **Computing Optimal Rotation** – Currently we compute the optimal rotation using a brute force approach improved with a Fourier transform. As the number of rotational symmetries tend to be very limited, it could be substantially improved either within the Fourier transform or by using a better approach for maximizing our optimization function [27].

# Appendix A

## Appendices

### A.1 Shapelet Proofs

#### A.1.1 Lemma 1

Polar shapelets form a set of steerable filters.

*Proof of Lemma 1.* The steerability of a more general class of filters that includes polar shapelets is presented. Suppose we have a function in polar coordinates of the form  $F(r, \theta) = f(r)g(\theta)$  where  $g(\theta) = e^{-ik\theta} = \cos(k\theta) - \imath \sin(k\theta)$  and with  $k$  as its  $k$ -fold symmetry. The same function, rotated by  $\varphi$ , is given by

$$F(r, \theta + \varphi) = f(r)g(\theta + \varphi) \tag{A.1}$$

since  $f$  is radially symmetric and is unaffected by the rotation. Expanding  $g$  using trigonometric identities gives

$$= e^{-ik(\theta + \varphi)} \tag{A.2}$$

$$= e^{-ik\theta} e^{-ik\varphi} \tag{A.3}$$

$$= e^{-ik\theta} (\cos(k\varphi) + \imath \sin(k\varphi)) \tag{A.4}$$

$$= \cos(k\varphi) e^{-ik\theta} + \imath \sin(k\varphi) e^{-ik\theta} \tag{A.5}$$

Substituting into  $F$ , we have

$$F(r, \theta + \varphi) = f(r)g(\theta + \varphi) \quad (\text{A.6})$$

$$= f(r)[\cos(k\varphi)g(\theta) - \imath \sin(k\varphi)g(\theta)] \quad (\text{A.7})$$

$$= \cos(k\varphi)f(r)g(\theta) - \imath \sin(k\varphi)f(r)g(\theta) \quad (\text{A.8})$$

$$= \cos(k\varphi)F(r, \theta) - \imath \sin(k\varphi)F(r, \theta). \quad (\text{A.9})$$

Taking just the real part gives

$$\Re[F(r, \theta + \varphi)] = \Re[\cos(k\varphi)F(r, \theta) - \imath \sin(k\varphi)F(r, \theta)] \quad (\text{A.10})$$

$$= \cos(k\varphi)\Re[F(r, \theta)] + \sin(k\varphi)\Im[F(r, \theta)]. \quad (\text{A.11})$$

Since  $S_{n,m}^\circ(r, \theta; \beta)$  has the same form as  $F$ , i.e. the product of a function of  $r$  with a complex exponential in  $\theta$ , we have

$$S_{n,m}^\circ(r, \theta + \varphi; \beta) = \cos(m\varphi) \Re[S_{n,m}^\circ(r, \theta; \beta)] + \sin(m\varphi) \Im[S_{n,m}^\circ(r, \theta; \beta)] \quad (\text{A.12})$$

and by simple change of coordinates we have

$$\Re[S_{n,m}^\circ(x, y; \beta, \varphi)] = \cos(m\varphi) \Re[S_{n,m}^\circ(x, y; \beta)] + \sin(m\varphi) \Im[S_{n,m}^\circ(x, y; \beta)]. \quad (\text{A.13})$$

□

## A.1.2 Lemma 2

A Shapelet's optimal orientation can be evaluated using  $\arctan\left(\frac{\Im\{S_{n,m}^\circ(r, \theta; \beta)\}}{\Re\{S_{n,m}^\circ(r, \theta; \beta)\}}\right)$

*Proof.*

$$\Re\left\{\frac{\delta}{\delta\phi}S_{m,n}^\circ(r, \theta - \phi; \beta)\right\} = \Re\{iS_{m,n}^\circ(r; \beta)e^{-i(m\theta - \phi)}\} = 0 \quad (\text{A.14})$$

$$= -S_{n,m}^\circ(r; \beta) \sin(m\theta - \phi) = 0 \quad (\text{A.15})$$

$$= S_{n,m}^\circ(r; \beta) (\cos(m\theta) \sin(\phi) - \sin(m\theta) \cos(\phi)) = 0 \quad (\text{A.16})$$

$$\Rightarrow \Im\{S_{m,n}^\circ(r, \theta; \beta)\} \cos(\phi) = \Re\{S_{n,m}^\circ(r, \theta; \beta)\} \sin(\phi) \quad (\text{A.17})$$

$$\phi = \arctan\left(\frac{\Im\{S_{n,m}^\circ(r, \theta; \beta)\}}{\Re\{S_{n,m}^\circ(r, \theta; \beta)\}}\right) \quad (\text{A.18})$$

□

*Proof of Lemma 2.* We prove the inner product between two normalized shapelets of the same type and scale is equal to the cosine of the difference of their orientations.

$$\int_{r,\theta} \Re \{S_{n,m}^\circ(r, \theta + \phi; \beta)\} \Re \{S_{n,m}^\circ(r, \theta; \beta)\} \quad (\text{A.19})$$

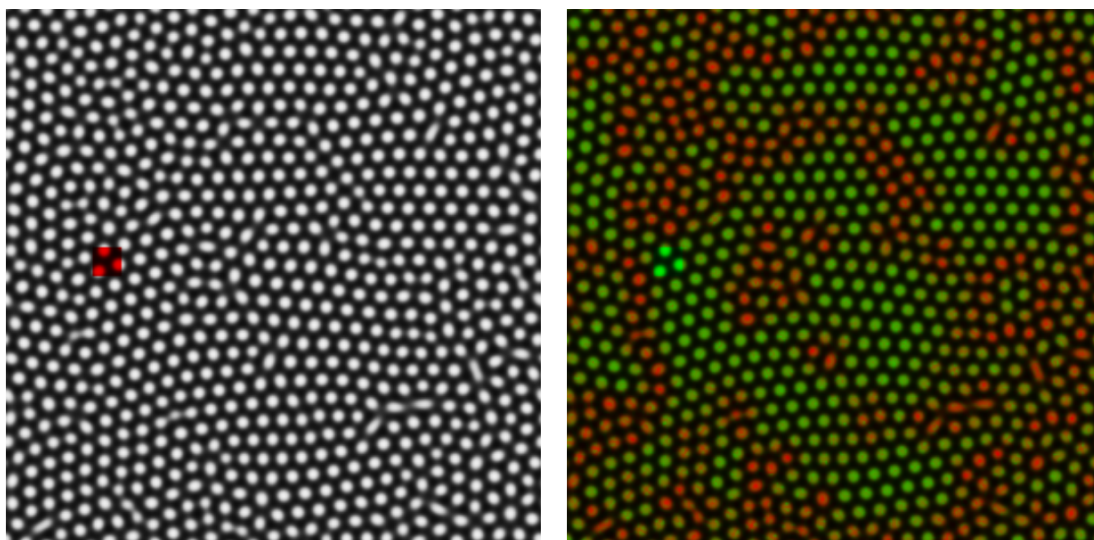
$$= \int_{r,\theta} S_{n,m}^\circ(r; \beta)^2 (\cos(m\theta + \phi) \cos(m\theta)) \quad (\text{A.20})$$

$$= \int_{r,\theta} S_{n,m}^\circ(r; \beta)^2 (\cos^2(m\theta) \cos(\phi) + \sin(m\theta) \cos(m\theta) \sin(\phi)) \quad (\text{A.21})$$

$$= \int_{r,\theta} S_{n,m}^\circ(r; \beta)^2 \cos^2(m\theta) \cos(\phi) = \cos(\phi) \quad (\text{A.22})$$

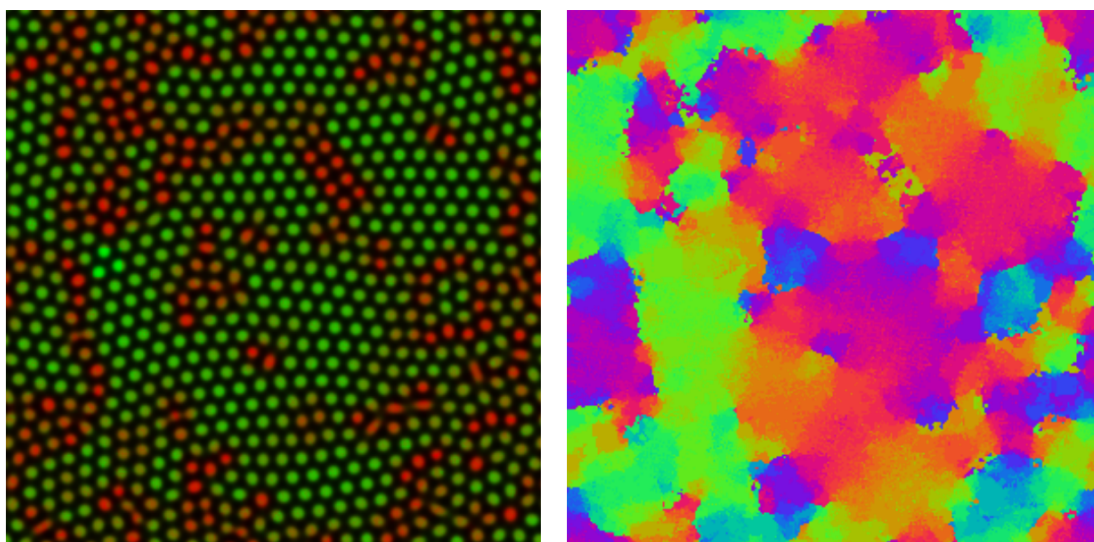
□

## A.2 Additional Sample Images



(a) Pattern with red sample region

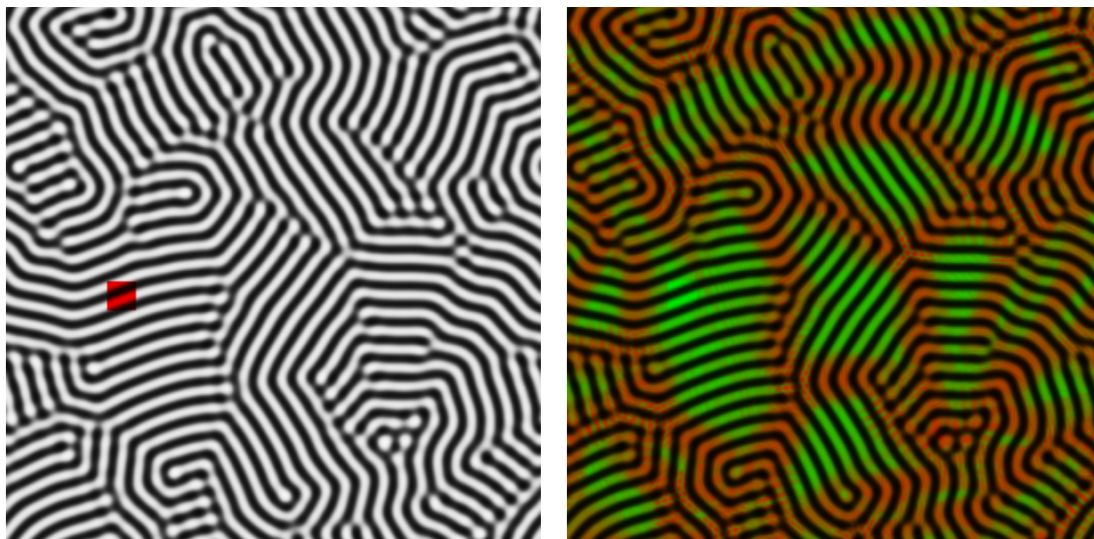
(b) Rotationally Insensitive Error Overlay



(c) Rotationally Sensitive Error Overlay

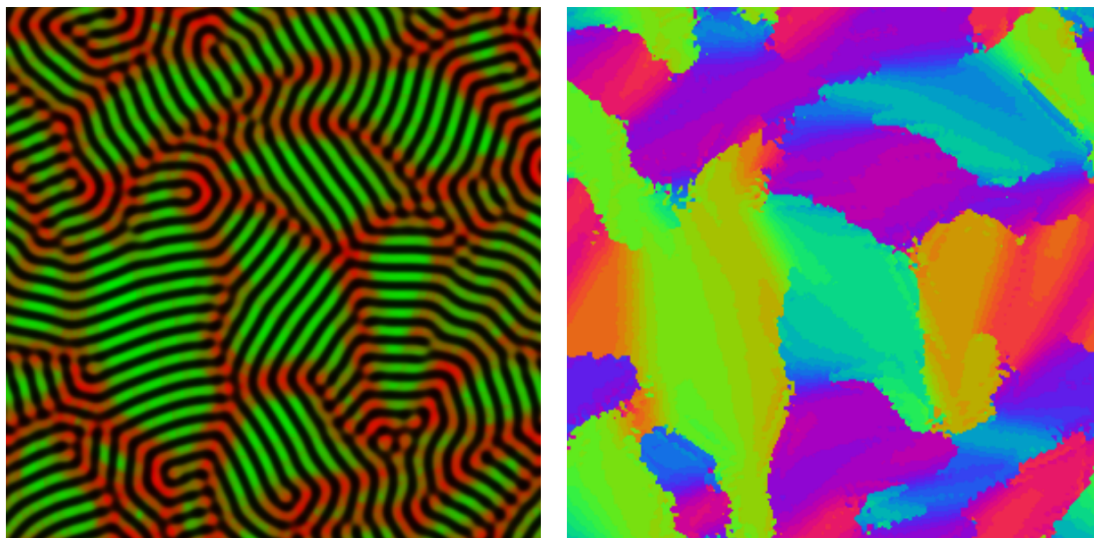
(d) Rotationally Sensitive Orientation

Figure A.1: A hexagonal pattern formed in a simulation of surface self assembly. This figure provides a comparison between the Chapter 3 and Chapter 4 approaches.



(a) Pattern with red sample region

(b) Rotationally Insensitive Error Overlay



(c) Rotationally Sensitive Error Overlay

(d) Rotationally Sensitive Orientation

Figure A.2: A striped pattern formed in a simulation of surface self assembly. This figure provides a comparison between the Chapter 3 and Chapter 4 approaches.

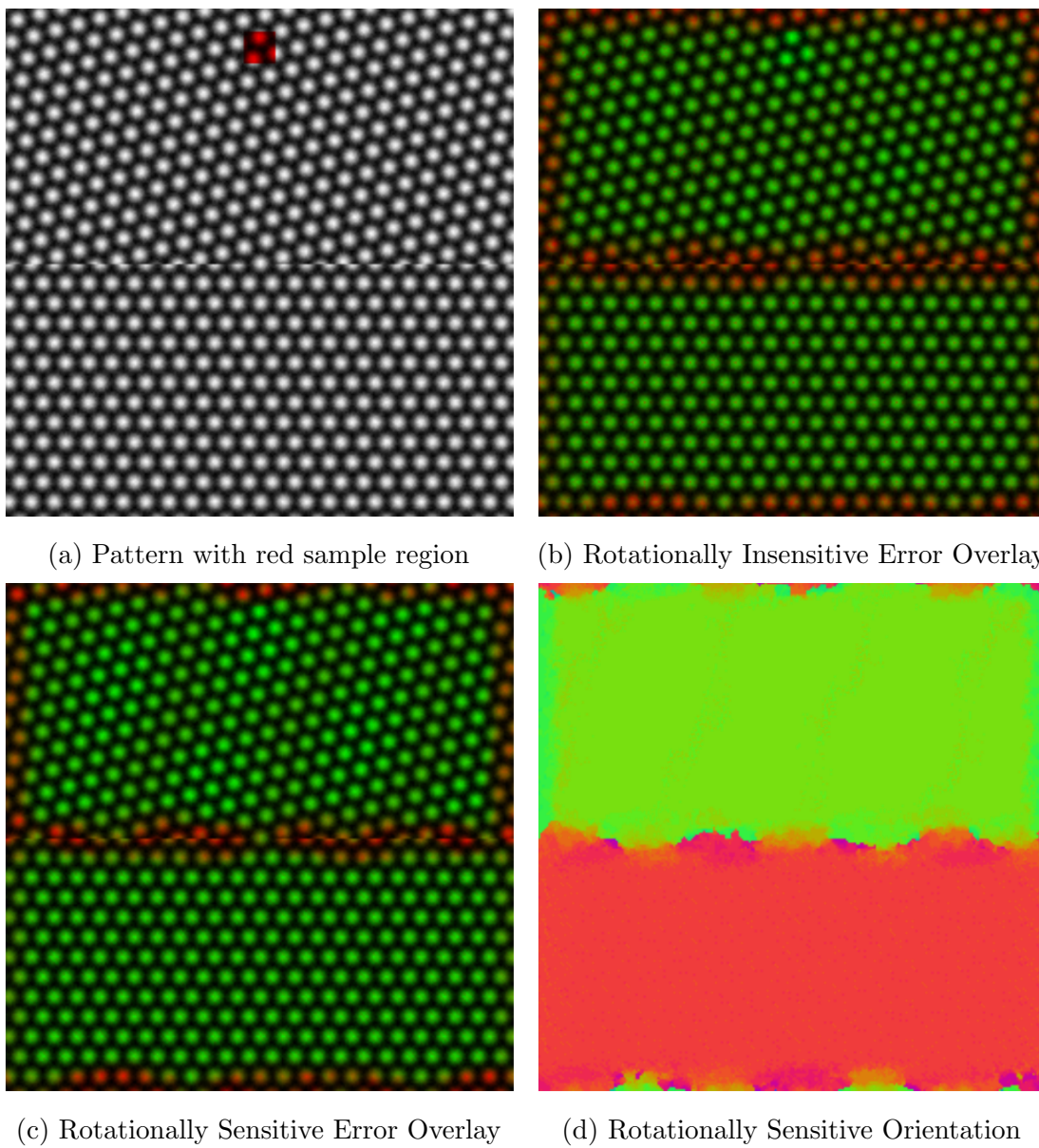
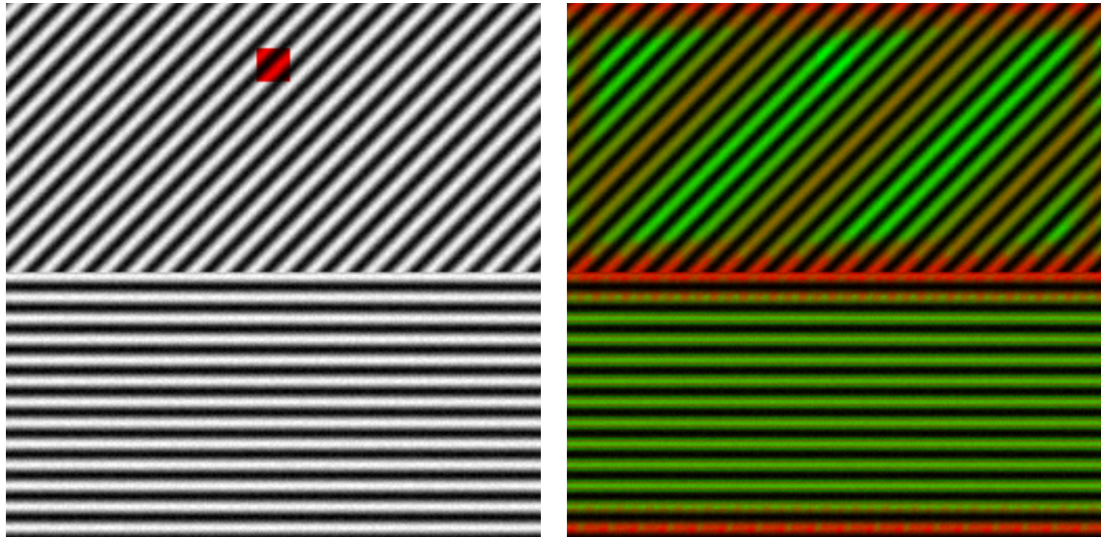
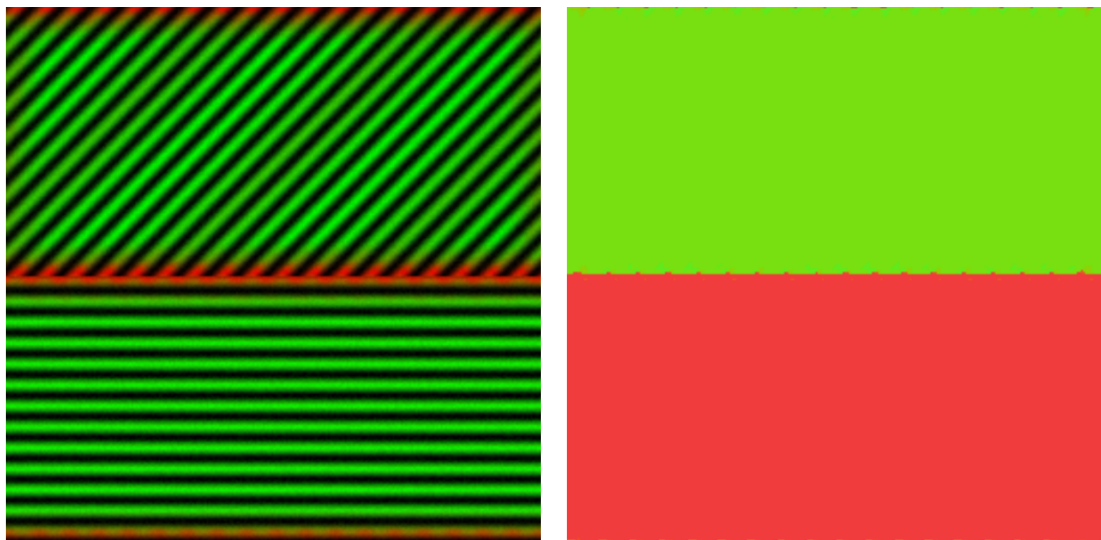


Figure A.3: A synthetically generated hexagonal pattern with changing orientation. This figure provides a comparison between the Chapter 3 and Chapter 4 approaches.



(a) Pattern with red sample region

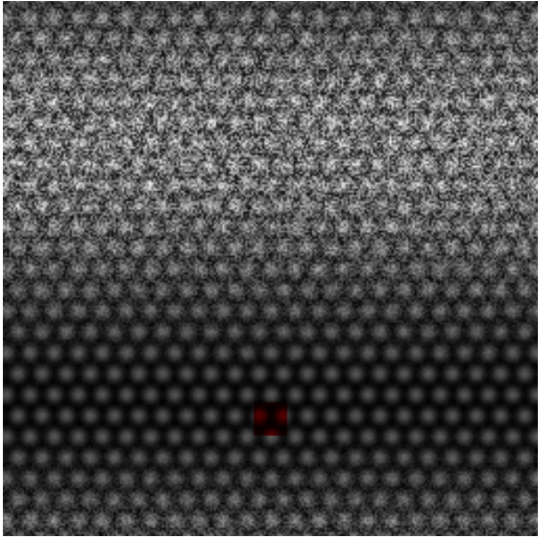
(b) Rotationally Insensitive Error Overlay



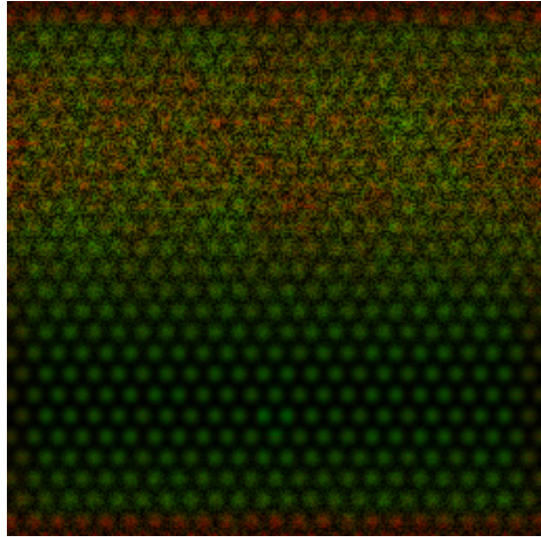
(c) Rotationally Sensitive Error Overlay

(d) Rotationally Sensitive Orientation

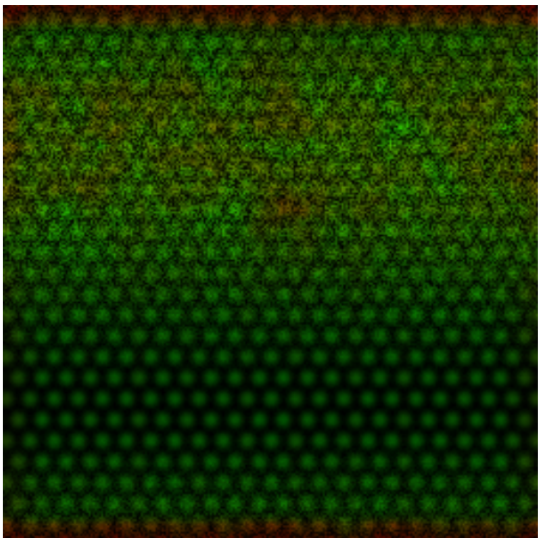
Figure A.4: A synthetically generated striped pattern with changing orientation. This figure provides a comparison between the Chapter 3 and Chapter 4 approaches.



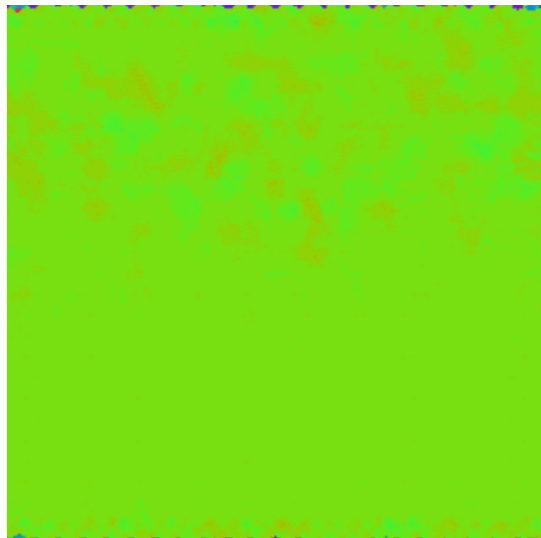
(a) Pattern with red sample region



(b) Rotationally Insensitive Error Overlay

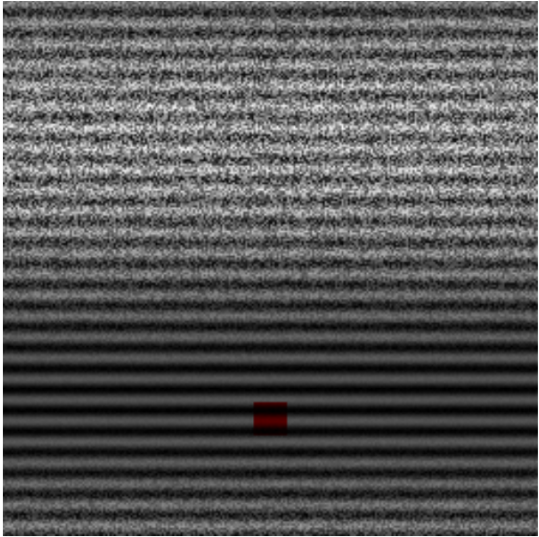


(c) Rotationally Sensitive Error Overlay

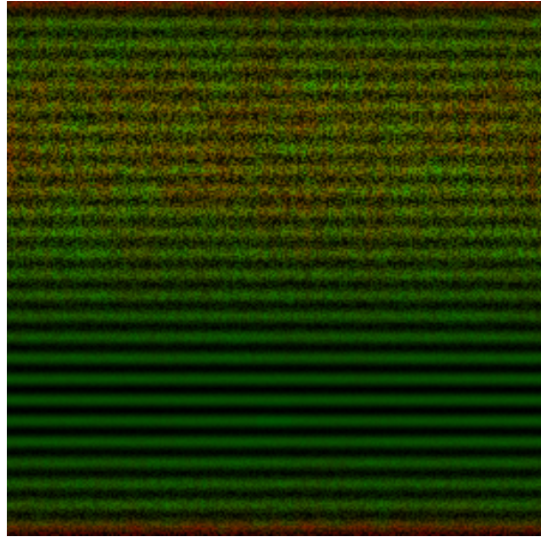


(d) Rotationally Sensitive Orientation

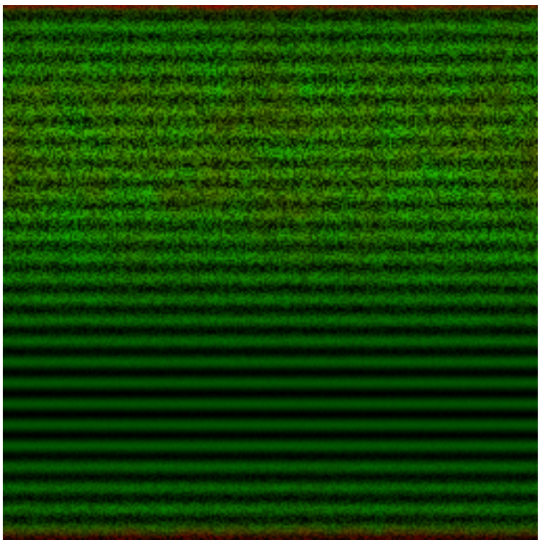
Figure A.5: A synthetically generated hexagonal pattern with varying noise. This figure provides a comparison between the Chapter 3 and Chapter 4 approaches.



(a) Pattern with red sample region



(b) Rotationally Insensitive Error Overlay

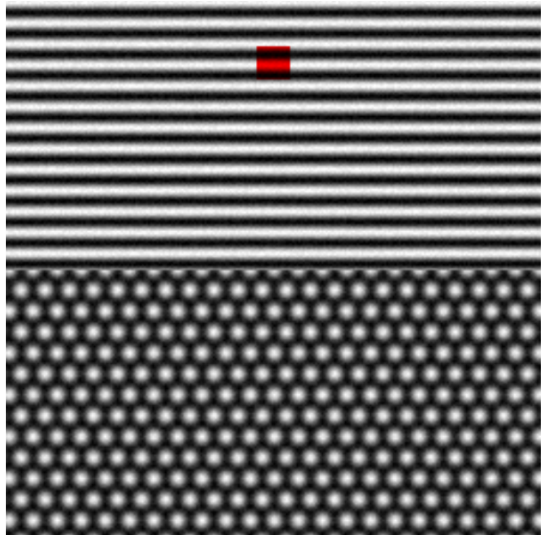


(c) Rotationally Sensitive Error Overlay

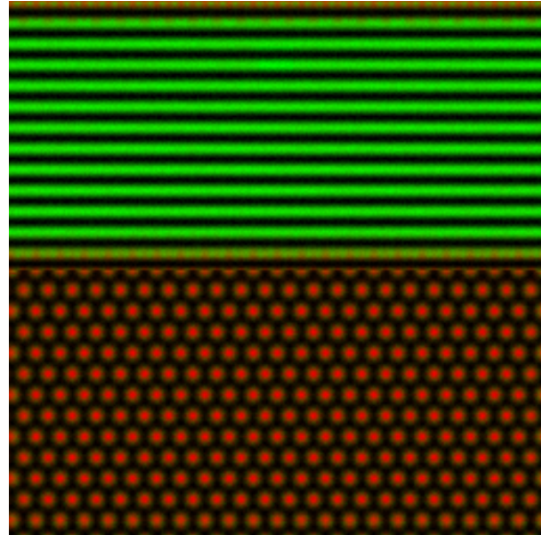


(d) Rotationally Sensitive Orientation

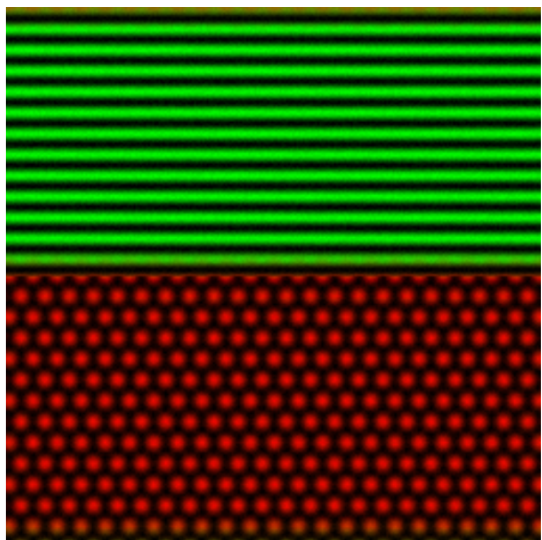
Figure A.6: A synthetically generated striped pattern with varying noise. This figure provides a comparison between the Chapter 3 and Chapter 4 approaches.



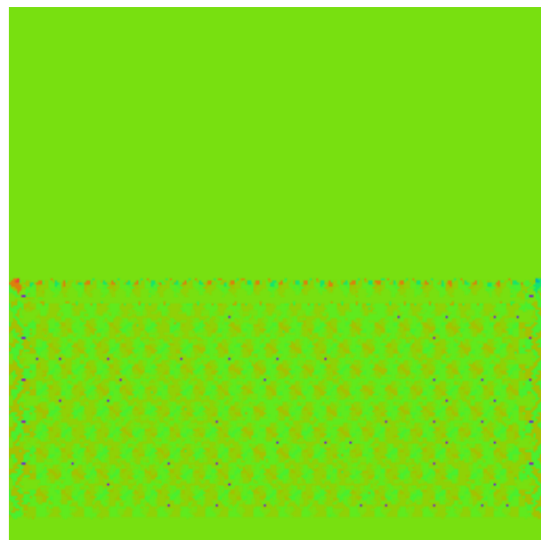
(a) Pattern with red sample region



(b) Rotationally Insensitive Error Overlay

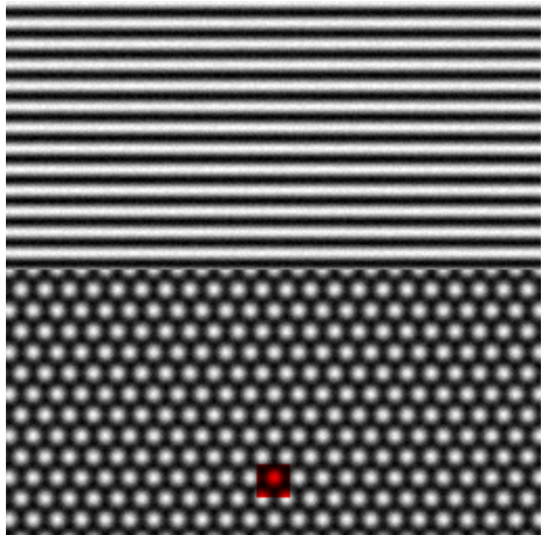


(c) Rotationally Sensitive Error Overlay

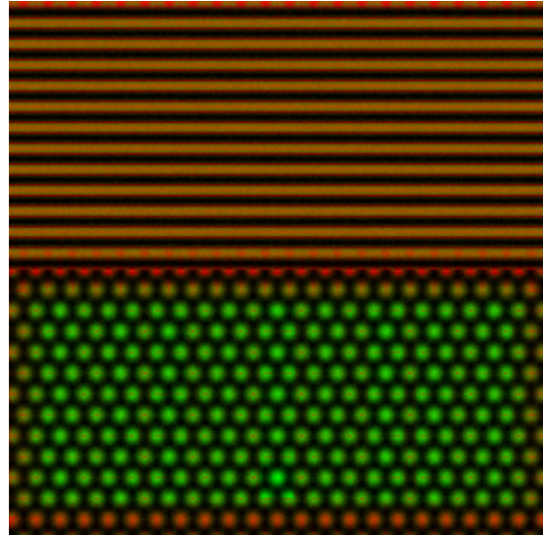


(d) Rotationally Sensitive Orientation

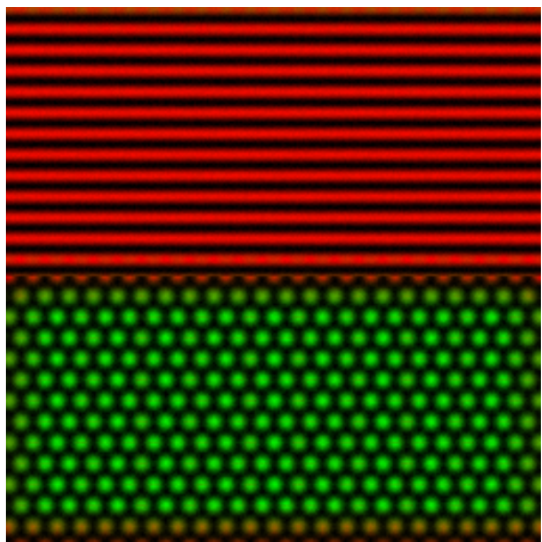
Figure A.7: A synthetically generated image containing both a striped and hexagonal pattern. This figure provides a comparison between the Chapter 3 and Chapter 4 approaches.



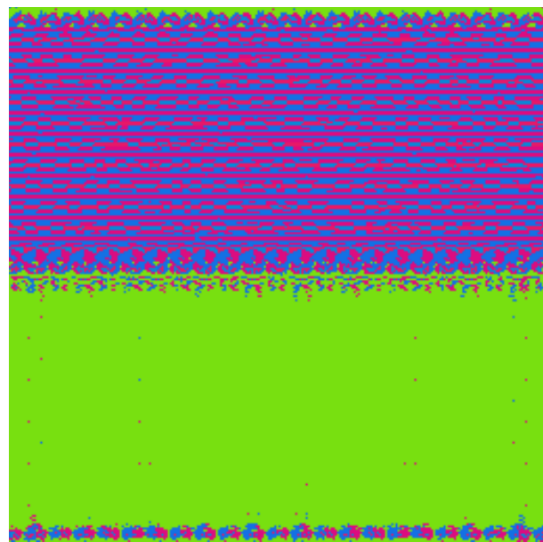
(a) Pattern with red sample region



(b) Rotationally Insensitive Error Overlay



(c) Rotationally Sensitive Error Overlay



(d) Rotationally Sensitive Orientation

Figure A.8: A synthetically generated image containing both a striped and hexagonal pattern with a different pattern sample. This figure provides a comparison between the Chapter 3 and Chapter 4 approaches.

# References

- [1] Katherine Jo Strandburg, editor. *Bond-orientational Order in Condensed Matter Systems*. Springer-Verlag, 1992.
- [2] Joy Y Cheng, Caroline A Ross, Henry I Smith, and Edwin L Thomas. Templated self-assembly of block copolymers: Top-down helps bottom-up. *Advanced Materials*, 18(19):2505–2521, 2006.
- [3] Song Xu, Sylvain JN Cruchon-Dupeyrat, Jayne C Garno, Gang-Yu Liu, G Kane Jennings, Tseh-Hwan Yong, and Paul E Laibinis. In situ studies of thiol self-assembly on gold from solution using atomic force microscopy. *Journal of Chemical Physics*, 108:5002–5012, 1998.
- [4] Steven De Feyter and Frans C De Schryver. Two-dimensional supramolecular self-assembly probed by scanning tunneling microscopy. *Chemical Society Reviews*, 32(3):139–150, 2003.
- [5] Pietro Artoni, Alessia Irrera, Emanuele Francesco Pecora, Simona Boninelli, Corrado Spinella, and Francesco Priolo. Heteroepitaxial growth of ge nanowires on si substrates. *International Journal of Photoenergy*, 2012, 2012.
- [6] David R Nelson and John Toner. Bond-orientational order, dislocation loops, and melting of solids and smectic-a liquid crystals. *Physical Review B*, 24(1):363, 1981.
- [7] Nasser Mohieddin Abukhdeir and Dionisios G. Vlachos. Nanoscale Surface Pattern Evolution in Heteroepitaxial Bimetallic Films. *ACS Nano*, 5(9):7168–7175, 2011.
- [8] Christopher Harrison, Douglas H. Adamson, Zhengdong Cheng, John M. Sebastian, Srinivasan Sethuraman, David A. Huse, Richard A. Register, and P. M. Chaikin. Mechanisms of Ordering in Striped Patterns. *Science*, 290(5496):1558–1560, 2000.

- [9] Y. Yokojima and Y. Shiwa. Hydrodynamic Interactions in Ordering Process of Two-dimensional Quenched Block Copolymers. *Phys. Rev. E*, 65(5):056308, May 2002.
- [10] C. Harrison, DE Angelescu, M. Trawick, Z. Cheng, DA Huse, PM Chaikin, DA Vega, JM Sebastian, RA Register, and DH Adamson. Pattern Coarsening in a 2D Hexagonal System. *EPL (Europhysics Letters)*, 67:800, 2004.
- [11] Nasser Mohieddin Abukhdeir and Alejandro D. Rey. Defect kinetics and dynamics of pattern coarsening in a two-dimensional smectic-A system. *New Journal of Physics*, 10(6):063025 (17pp), 2008.
- [12] S. Rehse, K. Mecke, and R. Magerle. Characterization of the dynamics of block copolymer microdomains with local morphological measures. *Phys. Rev. E*, 77(5):051805, May 2008.
- [13] Nasser Mohieddin Abukhdeir, Dionisios G. Vlachos, Markos Katsoulakis, and Michael Plexousakis. Long-time Integration Methods for Mesoscopic Models of Pattern-forming Systems. *Journal of Computational Physics*, 230(14):5704 – 5715, 2011.
- [14] R.J. Suderman, D. Lizotte, and N.M. Abukhdeir. Theory and application of shapelets to the analysis of surface self-assembly imaging. *Journal of Computational Physics*, 2014. submitted.
- [15] Alexandre Refregier. Shapelets i. a method for image analysis. *Monthly Notices of the Royal Astronomical Society*, 338(1):35–47, 2003.
- [16] Richard Massey and Alexandre Refregier. Polar shapelets. *Monthly Notices of the Royal Astronomical Society*, 363(1):197–210, 2005.
- [17] William T. Freeman and Edward H. Adelson. The design and use of steerable filters. *IEEE Transactions on Pattern Analysis and Machine Intelligence*, 13:891–906, 1991.
- [18] J. McGill, N.M. Abukhdeir, B.A. Ogunnaike, and D.G. Vlachos. Analysis and control of heteroepitaxial systems. *Journal of Process Control*, 2014. submitted, Special Issue on Control of Self-Assembly.
- [19] J.P. Boyd. *Chebyshev and Fourier spectral methods*. Dover Pubns, 2001.
- [20] D. Sundararajan. *The discrete fourier transform: theory, algorithms and applications*. World Scientific, 2001.

- [21] Jeff Orchard. Efficient global weighted least-squares translation registration in the frequency domain. In *Image Analysis and Recognition*, pages 116–124. Springer, 2005.
- [22] Pietro Perona. Deformable kernels for early vision. *IEEE Trans. Pattern Anal. Mach. Intell.*, 17(5):488–499, May 1995.
- [23] N. M. Abukhdeir. Bond-Orientational Order Recognition Library.
- [24] William S. Cleveland. Robust locally weighted regression and smoothing scatterplots. *J. Amer. Statist. Assoc.*, 74(368):829–836, 1979.
- [25] Gemunu H Gunaratne, Qi Ouyang, and Harry L Swinney. Pattern formation in the presence of symmetries. *Physical Review E*, 50(4):2802, 1994.
- [26] Joel D. Brock. Bond-Orientational Order. In Strandburg [1].
- [27] Jeff Orchard. Efficient least squares multimodal registration with a globally exhaustive alignment search. *Image Processing, IEEE Transactions on*, 16(10):2526–2534, 2007.